IEEE Open Journal of the
Industrial Electronics Society

Received 16 April 2024; revised 28 May 2024; accepted 14 June 2024. Date of publication 26 June 2024;
date of current version 8 July 2024. The review of this article was arranged by Associate Editor Yang Shi.

Digital Object Identifier 10.1109/OJIES.2024.3419422

Delayed Bilateral Teleoperation of Mobile Manipulators With Hybrid Mapping: Rate/Nonlinear-Position Modes

FERNANDO A. CHICAIZA [1], EMANUEL SLAWIÑSKI [2], AND VICENTE MUT [2]

[1]Centro de Investigación de Ciencias Humanas y de la Educación, Universidad Indoamérica Ambato 180103, Ecuador
[2]Instituto de Automática, Universidad Nacional de San Juan San Juan 5400, Argentina

CORRESPONDING AUTHOR: FERNANDO A. CHICAIZA, (e-mail: fachicaiza@indoamerica.edu.ec).

This work was supported in part by the UNSJ-CONICET, Argentina, in part by the German Academic Exchange Service (DAAD) under Grant 91730325, and in part by the Universidad Indoamérica del Ecuador.

ABSTRACT Mobile manipulators find versatile applications across various fields, leveraging the combination of autonomous functionalities and bilateral teleoperation schemes to enhance the effectiveness of these robotic mechanisms. Regarding teleoperation, command generation involves a leader robot with a few degrees of freedom in a bounded workspace, accompanied by a redundant follower robot operating in an unbounded workspace. This article introduces the concept of Cartesian/articular control for delayed bilateral teleoperation of a mobile manipulator, where the follower robot aims to execute the rate/nonlinear-position commands issued by a human handling the leader robot through a proposed hybrid mapping. We implement a P+d controller applied in Cartesian space for the leader while a controller based on inverse kinematics in joint space is employed for the follower, taking advantage of its redundancy. We then propose a Lyapunov–Krasovskii candidate function to analyze theoretically and numerically the time derivative of the functional on the system trajectories. As a result, we derive the conditions that the proposed hybrid mapping and controller parameters must satisfy to ensure bounded errors. Finally, we statistically evaluated objective metrics from multiple pick-and-place task executions considering time delays to quantify the performance achieved.

INDEX TERMS Bilateral teleoperation, Lyapunov–Krasovskii, mobile manipulator, rate-position mapping.

NOMENCLATURE

Scalars:

m, n	Leader and follower DoF.
α_m, α_s	Damping gain constants for controllers.
k_m, k_p	Proportional gain constants for controllers.
$k_1, k_2, k_3, k_4, \eta, \gamma$	Lyapunov–Krasovskii function constants.
k_a, k_b, k_g	Gain constants for rate/NL-position references.
t_c, t_{c+1}	Initial and final transition time between modes.
h_1, h_2	Forward and backward delays.
c	Number of transition between modes.
V	Lyapunov–Krasovskii function candidate.
Δ_{rp}	Transition period when changing modes.
χ	Coriolis matrix bound.
E_h, E_e	Human and environment energies.

Functions:

$\varepsilon(t), \beta(t)$	Functions to transition between rate and NL-position modes.
$\dot{\varepsilon}(t), \dot{\beta}(t), \xi$	Derivative of the functions to transition between modes and its upper bound.

Vectors:

$\mathbf{x_m}, \dot{\mathbf{x}}_\mathbf{m}, \ddot{\mathbf{x}}_\mathbf{m} \in \mathbb{R}^m$	Position, velocity, and acceleration of the leader robot in the Cartesian space.

$\mathbf{x_s}, \dot{\mathbf{x}}_\mathbf{s}, \ddot{\mathbf{x}}_\mathbf{s} \in \mathbb{R}^m$	Position, velocity, and acceleration of the follower robot in the Cartesian space.
$\mathbf{q_s}, \dot{\mathbf{q}}_\mathbf{s}, \ddot{\mathbf{q}}_\mathbf{s} \in \mathbb{R}^n$	Position, velocity, and acceleration of the follower robot in the articular space.
$\mathbf{g_m} \in \mathbb{R}^m, \mathbf{g_s} \in \mathbb{R}^n$	Gravity vector for the leader and follower robot.
$\mathbf{f_m}, \mathbf{f_h}, \mathbf{f_e} \in \mathbb{R}^m$	Leader, human, and environment Cartesian forces.
$\boldsymbol{\tau_s}, \boldsymbol{\tau_e} \in \mathbb{R}^n$	Follower and environment articular torques.
$\mathbf{f_p}(.) \in \mathbb{R}^m$	Nonlinear-position mapping function.
$\mathbf{ref}, \dot{\mathbf{ref}} \in \mathbb{R}^m$	Function linking rate and nonlinear-mapping modes and its derivative.
$\mathbf{e}, \dot{\mathbf{e}} \in \mathbb{R}^m$	Coordination error and its derivative.
$\boldsymbol{\gamma} \in \mathbb{R}^m$	Transition between modes effect.
$\boldsymbol{\Upsilon_1}, \boldsymbol{\Upsilon_2} \in \mathbb{R}^m$	Nonlinear and linear perturbations.
Matrices:	
$\mathbf{M_m}, \mathbf{C_m} \in \mathbb{R}^{m\times m}$	Leader's inertia and centripetal and Coriolis forces.
$\mathbf{M_s}, \mathbf{C_s} \in \mathbb{R}^{n\times n}$	Follower's inertia and centripetal and Coriolis forces.
$\mathbf{J}, \mathbf{J_D} \in \mathbb{R}^{n\times n}$	Follower raw and damped Jacobian.
$\mathbf{W} \in \mathbb{R}^{n\times n}$	Weighting matrix.
$\nabla_\mathbf{fp} \in \mathbb{R}^{m\times m}$	Nonlinear-mapping function's gradient.
$\mathbf{P} \in \mathbb{R}^{m\times m}$	Gain matrix.

I. INTRODUCTION

Teleoperation systems enable the extension of human manipulation and navigation capabilities across different scales, facilitating interaction with remote or hazardous environments [1], [2]. An increasingly utilized type of robot is the mobile manipulator, a mechanism that combines the mobility of a mobile robot with the manipulation capabilities of a robotic arm [3]. These systems are versatile and find applications across various industries [4]. Mobile manipulators are employed in diverse fields such as manufacturing, logistics, warehousing, agriculture, construction, healthcare assistance, inspection and maintenance, and the delivery of goods and services, among others [5]. Depending on the task and the location of the working environment, mobile manipulators follow commands generated through the processing of sensor information and set objectives (automatic control), references sent from a remote station (teleoperated control), or a combination of both. In bilateral teleoperated control, several considerations must be taken into account when designing the control scheme. These include the control mode of the follower robot with a mobile part and the robotic arm, workspaces of the robots considering the disparity between mechanisms, time delays produced by the communication channel, haptic feedback, and other relevant factors.

The strategies employed in teleoperating mobile manipulators, as identified in the current state of the art, can be summarized as follows: a) managing the robotic arm in position control and the mobile platform in rate mode separately, using either two devices or a single device that switches to operate each part; or b) sending velocity references to the operating end, as demonstrated in [6]. In this article, we adopt an approach akin to b), treating the follower robot as a unified mechanism. This allows us to capitalize on the redundancy inherent in mobile manipulators. To achieve this unified control, we consider the inherent disparity between the local and remote robots. The local robot, serving as the manipulator, is constrained by a limited workspace, typically associated with the reach of a human operator's arm. In contrast, the remote robot represents a highly redundant mechanism with a practically infinite workspace, limited only by the height the manipulator can reach.

From the literature, two common approaches are proposed for teleoperating robots with different workspaces: 1) position and 2) rate mapping. The conventional solution involves scaling the leader haptic device's workspace to match the task space, enabling the human operator to interact with remote environments at scale. However, position-mode control faces a resolution challenge when accurately placing the follower in the presence of a substantial disparity in workspace between leader and follower [7]. While linear mappings are frequently used in position mode, this option represents a specific case within the broader category of potential nonlinear mappings, including those leveraging artificial intelligence techniques. An alternative approach is to utilize rate (velocity) mode, where the follower's velocity corresponds to the leader's displacement. Rate mode control has demonstrated its suitability for the follower's operation in free motion, allowing it to cover large workspaces. Nevertheless, operating a robot in rate mode presents significant stability limitations and transparency issues when in contact with the environment [8]. In addressing this concern, a proposed solution incorporates both scaled-position and rate in its internal structure, aiming to exploit the advantages of both methods, where the transition between modes is a crucial consideration in the design process [9], [10].

Transition, in this context, refers to the activation of modes, whether through switching or continuous adjustment. Given that the command mapping involves both position and rate, the transition between these modes significantly impacts the overall stability of the system. In addressing this aspect, various proposals lean toward discrete switching between modes due to its ease of implementation. This can be achieved through external events, such as button presses, or internal events, like defining zones within the leader's workspace [11], [12]. On the other hand, continuous transitions between modes can be facilitated by using derivable functions such as sigmoids, as demonstrated in [8].

Furthermore, time delays between the remote robot and the haptic device can produce a low performance of the bilateral teleoperation system. Consequently, the stability of the coordination error and velocities must be analyzed by introducing some control scheme, placed on both haptic device and remote robot, to mitigate such effects [13]. Although to date it is not standardized which is the optimal control scheme for bilateral teleoperation systems with time delays, there are many

TABLE 1. Related Works in Literature

Authors	Method	Leader Centering	Haptic Feedback	Transition	Switch trigger	Performance Analysis	Stability Analysis	Time delay analysis
Barrio et al. [18]	Position / Rate	At starting, when changing from rate to position	When changing modes, proportional to the rate command	Discrete using a hysteresis area between modes	Via leader workspace	Comparing position/rate vs. scaled position	No	No
Khalifa et al. [20]	Position / Rate	Manually	No	Discrete	Using a leader button	No	No	No
Liu et al. [11]	Variable scaled position / rate	Manually, dead zone considered	Proportional to rate and scaled position	Discrete	Using Keyboard	Comparing hybrid, rate and scaled position control	No	No
Voskuil. [9]	Scaled position / rate	Manually	Force exerted by the follower on the environment	Discrete	Via leader workspace	Comparing with scaled position	No	No
Bu et al. [12]	Position/Rate	Pressing a button	Based on three and four channel structure	Discrete	Via leader workspace zones & leader button	No	No	No
Pepe et al. [21]	Position/Rate	Manually	Based on elastic force	Continuous	Via leader workspace	No	No	No
Liu et al. [22]	Mapping based on a variable scaled leader position	Manually	Based on stiffness of the environment	Depending on the mapping function	Depending on the mapping function	Comparing motion mapping	No	No
Mokogwu et al. [8]	Position/Rate	Manually	Force exerted by the follower on the environment	Continuous	Based on task workspace, by sigmoid function	Based on transparency	Based on passivity theory	No
Gou et al. [23]	Position/Edge drifting algorithm	Manually	None	Continuous	Manually	Based on objective measurements	No	No
Han et al. [19]	Position/Rate	Manually	When reaching constrains	Continuous	Via control mode selector	Based on objective and subjective measurements	No	No
Li et al. [24]	Position/Rate	Manually	Based on artificial potential field and switching	Continuous	Based on comparing coefficients	Based on objective and subjective measurements	No	No

alternatives that can be applied to manipulator and mobile robots such as wave variables [14], artificial-intelligence-based techniques [15], passivity-based control [16], P+d techniques [17], among others. In general, most techniques are calibrated depending on the time delay, for example, in the P+d strategy the damping level directly depends on the time delay magnitude. Moreover, the operator can receive either force feedback to alert a mode change, damping from the leader, or the force exerted by the follower when working in the environment [11], [18], [19]. Table 1 shows a summary of the state of the art, focusing mainly on manipulator robots and the gradual switch between modes of rate mapping and position linear mapping, without neglecting inherent parameters of teleoperation, such as time delays, bilateral system stability, and force feedback.

As shown in Table 1, the literature includes strategies for teleoperating a mobile manipulator, typically treating the follower robot as a system divided into its mobile base and the manipulator. Continuous switching between rate and position modes primarily depends on the position of the local robot's end-effector (E.E.) [21], [24]. However, we identified a weakness in the stability analysis of these teleoperation systems, which is necessary to understand the behavior of velocities and errors over time, especially when the communication channel may introduce time delays that can lead to discrepancies between local commands and remote system responses. To the best of our knowledge, the existing literature does not include a proposal for achieving a stable delayed bilateral teleoperation scheme for mobile manipulators, with rate/position transitions dependent on an additional degree of freedom rather than solely on the leader robot's position. Next, we state the main contributions of this article.

1) Formulation of a delayed bilateral teleoperation system, employing Cartesian control for the local robot and articular control for the redundant follower robot.
2) Proposal of a hybrid mapping function, integrating two commonly used teleoperation modes: 1) rate and 2) nonlinear position, with transitions mediated by an additional degree of freedom, creating a continuous and differentiable mapping that allows generating references using a bounded leader workspace to an unbounded follower workspace.
3) Stability analysis of the delayed bilateral teleoperated system, combining a study based on Lyapunov–Krasovskii theory with a numerical evaluation method.
4) Analysis of the required conditions for the rate/position mapping, the transition function between modes, and the parameters of the control scheme to ensure the boundedness of velocities and coordination error.
5) Testing of the proposed scheme, conducting a statistical evaluation of quantitative metrics, with human-in-the-loop experiments using a haptic device, communication equipment between the local and remote sites, and a dedicated computer running ROS2 and the Gazebo simulator. The results obtained are compared objectively with another strategy from the state of the art.

To validate the results obtained, human-in-the-loop experiments are conducted using a haptic device, communication

equipment between the local and remote sites, and a dedicated computer running ROS2 and the Gazebo simulator. The reported results for coordination error and velocities are computed considering tests with and without time delays, ultimately presenting objectively measured metrics and comparing them with a proposal from the literature.

The rest of the article is organized as follows: Section II introduces the models and assumptions and defines the control objective. Moreover, a comprehensive mapping is established, integrating rate and NL-position modes. Subsequently, Section III delves into stability analysis, providing detailed conditions alongside illustrative surface plots. Section IV outlines the experimental setup and showcases the results of human-in-the-loop simulations conducted. Finally, Section V concludes this article.

II. PRELIMINARY AND PROBLEM STATEMENT

A. NOTATION

If k is a scalar, $\mathbf{x}$ is a vector with its transpose $\mathbf{x}^{\mathbf{T}}$. $\mathbf{M}$ is a matrix with its transpose $\mathbf{M}^{\mathbf{T}}$ and its Moore–Penrose pseudoinverse $\mathbf{M}^{\dagger}$, $k\mathbf{x}$ is a vector $\mathbf{x}$ scaled by k, $|\mathbf{x}|$ and $\|\mathbf{x}\|$ represents the absolute value and the Euclidean norm of $\mathbf{x}$, respectively, and $\|\mathbf{M}\|$ stands for the infinity norm of matrix $\mathbf{M}$. $\dot{\mathbf{x}}$ and $\ddot{\mathbf{x}}$ represent the first and second derivatives of $\mathbf{x}$ respect to time. diag($\mathbf{x}$) generates a gain matrix $\mathbf{X}$ from the $\mathbf{x}$ vector.

B. PROPERTIES, ASSUMPTIONS, AND LEMMAS

Property 1: The inertia matrices $\mathbf{M_m}(\mathbf{x_m})$ and $\mathbf{M_s}(\mathbf{x_s})$ are symmetric positive definite, and it is known that

$$\lambda_{m_{min}}\mathbf{I} \leq \mathbf{M_m} \leq \lambda_{m_{max}}\mathbf{I}$$
$$\lambda_{s_{min}}\mathbf{I} \leq \mathbf{M_s} \leq \lambda_{s_{max}}\mathbf{I}.$$

Property 2: The matrices $\dot{\mathbf{M}}_{\mathbf{s}}(\mathbf{x_s}) - 2\mathbf{C_s}(\dot{\mathbf{x}}_{\mathbf{s}}, \mathbf{x_s})$, and $\dot{\mathbf{M}}_{\mathbf{m}}(\mathbf{x_m}) - 2\mathbf{C_m}(\dot{\mathbf{x}}_{\mathbf{m}}, \mathbf{x_m})$ are skew-symmetric, i.e.,

$$\dot{\mathbf{M}}_{\mathbf{m}}(\mathbf{x_m}) = \mathbf{C_m}(\dot{\mathbf{x}}_{\mathbf{m}}, \mathbf{x_m}) + \mathbf{C}_{\mathbf{m}}^{\mathbf{T}}(\dot{\mathbf{x}}_{\mathbf{m}}, \mathbf{x_m})$$
$$\dot{\mathbf{M}}_{\mathbf{s}}(\mathbf{x_s}) = \mathbf{C_s}(\dot{\mathbf{x}}_{\mathbf{s}}, \mathbf{x_s}) + \mathbf{C}_{\mathbf{s}}^{\mathbf{T}}(\dot{\mathbf{x}}_{\mathbf{s}}, \mathbf{x_s}).$$

Property 3: Defining a constant χ so that $\chi = \|\mathbf{P}\|$, where each element $(i, j)th$ of the matrix $\mathbf{P}$ is calculated from the uniform upper bound $\bar{c}_{kji}$ of the Christoffel symbols $c_{kji}(|c_{ijk}(q)| \leq \bar{c}_{kji})$

$$p_{ij} = \sqrt{\sum_{k=1}^{s}(\bar{c}_{kji})^2}$$

a uniform bounded of the Coriolis matrix can be proposed [25], i.e.,

$$\|\mathbf{C}(\dot{\mathbf{x}}, \mathbf{x})\| \leq \chi\|\dot{\mathbf{x}}\| \quad \forall \mathbf{x} \in \mathbb{R}^s.$$

Assumption 1: The human operator and the environment can be represented as follows [26]:

$$E_h = \phi_h - \int_0^t \mathbf{f_h}(\epsilon)^{\mathbf{T}}\dot{\mathbf{x}}_{\mathbf{m}}(\epsilon)d\epsilon \geqslant 0 \tag{1}$$

$$E_e = \phi_e - \int_0^t \mathbf{f_e}(\epsilon)^{\mathbf{T}}\dot{\mathbf{x}}_{\mathbf{s}}(\epsilon)d\epsilon \geqslant 0. \tag{2}$$

Moreover, we supposed that $\mathbf{f_h} \in \mathcal{L}_\infty$.

Assumption 2: The communication channel is represented by a forward $h_1(t)$ and a backward $h_2(t)$ time-varying delays. These time delays are considered bounded, i.e., $0 \leq h_1(t) \leq \bar{h}_1$ and $0 \leq h_2(t) \leq \bar{h}_2$ for all t. For this article, it is considered that the channel can store energy given the delays, but there is no loss of information.

Lemma 1: For real vector functions $\mathbf{a}(.)$ and $\mathbf{b}(.)$ and a time-varying scalar $h(t)$ with $0 \leq h(t) \leq \bar{h}$, the following inequality holds:

$$-2\mathbf{a}^{\mathbf{T}}(t)\int_{t-h(t)}^{t}\mathbf{b}(\rho)d(\rho) - \int_{t-h(t)}^{t}\mathbf{b}^{\mathbf{T}}(\rho)\mathbf{b}(\rho)d(\rho) \leq h(t)\mathbf{a}^{\mathbf{T}}(t)\mathbf{a}(t) \leq \bar{h}\mathbf{a}^{\mathbf{T}}(t)\mathbf{a}(t).$$

C. TELEOPERATION SCHEME AND MATHEMATICAL MODELING

Fig. 1 illustrates the complete bilateral teleoperation scheme, denoting both sites and the communication channel. To the left, the local site displays the interaction between the human operator and the haptic device, where the mapping of rate/NL-position commands is generated. To the right, the follower robot interacting with its working environment is shown, where the modified-Jacobian-based controller is applied. The communication channel allows for the transmission of both the mapping information (generated by the local site) and the position of the remote robot's E.E., both delayed by the influence of the technology used. The exchange of this information is used to calculate the Proportional+damping controllers for each robot. In this way, this section presents the design of references for rate and position modes, the mathematical representation of both robots and controllers.

1) RATE/NL-POSITION MAPPING MODE

Assuming that the transition between rate and nonlinear-position mapping modes is controlled via an ON/OFF degree of freedom (mode button), the operator can initiate the c_{th} mode transition at any time interval starting from t_c until the subsequent transition to $c+1$, where $c = 0, 1, 2, \ldots, j$. Therefore, considering adjustment constants k_a, k_b, and k_g, we present the mapping from leader position to follower reference formed by those two modes: a rate mapping part $k_a\int_{t_c}^{t_{c+1}}\tanh(k_b\mathbf{x_m})dt$ and a nonlinear-position mapping $k_g\mathbf{f_p}(\mathbf{x_m})$, additionally considering the current state at the time of the mode transition $\mathbf{ref}_{t_c}$. In this way, a continuous and differentiable reference is established as

$$\mathbf{ref} = \varepsilon(t)k_a\int_{t_c}^{t_{c+1}}\tanh(k_b\mathbf{x_m})dt + \beta(t)k_g\mathbf{f_p}(\mathbf{x_m}) + \mathbf{ref}_{t_c} \tag{3}$$

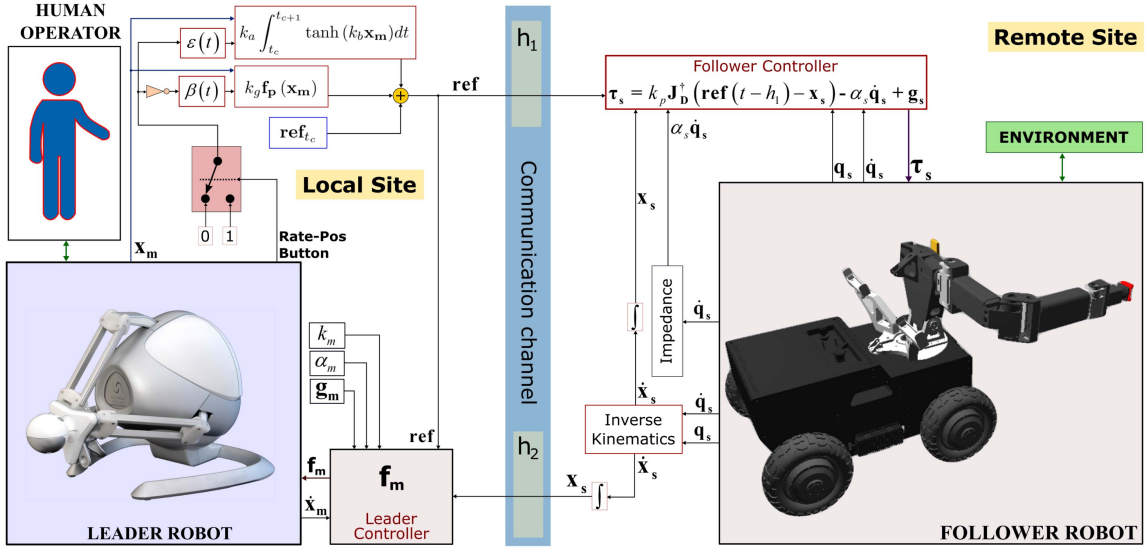

FIGURE 1. Bilateral teleoperation scheme with Rate/NL-Position mapping showing local site, remote site, and communication channel.

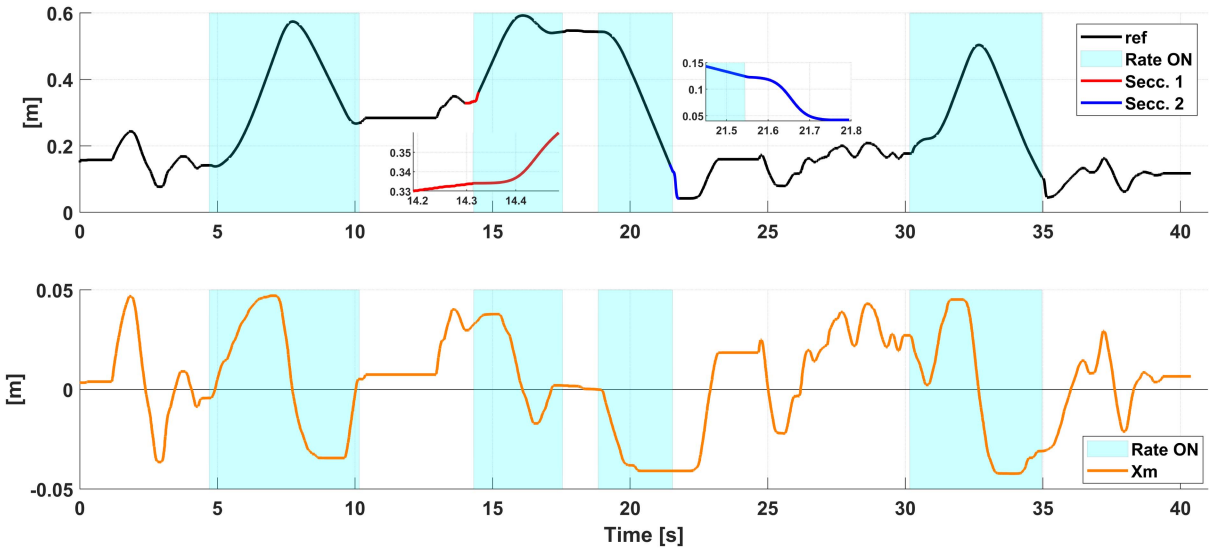

FIGURE 2. Generation of the mapping function ref to combine rate and NL-position modes. In the lower subplot: Behavior of one component of the leader's E.E. position shown in orange; in the upper subplot: mapping generated by the behavior of the local robot and the modes transition (highlighted in cyan).

where $\varepsilon(t)$ and $\beta(t)$ are continuous and differentiable functions whose output goes from 0 to 1 each time the mode button (rate/nonlinear-position) is pressed.

We define a minimum interval between transition Δ_{rp} such that $t_{c+1} - t_c \geqslant \Delta_{rp}$.

Fig. 2 facilitates the interpretation of transitions between the rate mode (highlighted in cyan) and NL-position mode. At the bottom, the behavior of one component of the leader's E.E. position is shown in orange. This variation of the local robot and the mode transition allows mapping the reference displayed in the upper subplot. Thus, the generated mapping is shown in black, with sections indicating: Secc.1) transition to rate mode (from $t = 14.2$ s to $t = 14.5$ s) and Secc.2) transition to NL-position mode (from $t = 21.4$ to $t = 21.8$ s). Both sections indicate the smooth transition generated by the functions $\varepsilon(t)$ and $\beta(t)$. Since $\mathbf{f_p}(\mathbf{x_m})$ used to exemplify the mapping is a scaled linear function, it can be observed in the position mode sections (e.g., from $t = 22$ to $t = 30$ s) that both **ref** and $\mathbf{x_m}$ are analogous.

Next, upon activating either the NL-position or rate mode, the dynamics of the mapping described in (3) is obtained as

$$\dot{\mathbf{ref}} = \dot{\varepsilon} k_a \int_{t_c}^{t_c+\Delta_{rp}} \tanh\left(k_b \mathbf{x_m}\right) dt + \varepsilon k_a \tanh\left(k_b \mathbf{x_m}\right) + \dot{\beta} k_g \mathbf{f_p}\left(\mathbf{x_m}\right) + \beta k_g \nabla_{\mathbf{fp}} \dot{\mathbf{x}}_\mathbf{m}.$$

Now, if in the last equation, we consider that both the dynamics of the function activating the rate mode $\varepsilon(t)$ and the function activating the position mode $\beta(t)$ are upper-bounded

by a constant ξ, i.e., $\dot{\varepsilon}, \dot{\beta} \leq \xi$, then

$$\mathbf{r\dot{e}f} \leqslant \xi \boldsymbol{\gamma} + \varepsilon k_a \tanh\left(k_b \mathbf{x_m}\right) + \beta k_g \nabla_{\mathbf{fp}} \dot{\mathbf{x}}_{\mathbf{m}} \tag{4}$$

where

$$\boldsymbol{\gamma} = k_a \int_{t_c}^{t_{c+\Delta rp}} \tanh\left(k_b \mathbf{x_m}\right) dt + k_g \mathbf{f_p}\left(\mathbf{x_m}\right).$$

In addition to merging the rate and nonlinear-position modes into a unified expression, the mapping function **ref** enables a continuous transition between modes through a discrete degree of freedom. This transition does not rely on $\mathbf{x_m}$ [21] (simplifying the control of the leader robot) or the state of the environment [27], thus facilitating its generalization to other applications. Furthermore, it also meets the necessary criteria for subsequent stability analysis of the system.

2) ROBOTS MODELING

According to the dynamic behavior [28] of the robots and using Euler–Lagrange modeling, the typical nonlinear dynamic model

$$\mathbf{M_s}(\mathbf{q_s})\ddot{\mathbf{q}}_{\mathbf{s}} + \mathbf{C_s}(\mathbf{q_s}, \dot{\mathbf{q}}_{\mathbf{s}})\dot{\mathbf{q}}_{\mathbf{s}} + \mathbf{g_s}(\mathbf{q_s}) = \boldsymbol{\tau}_{\mathbf{s}} + \mathbf{J}^{\mathbf{T}}\mathbf{f_e} \tag{5}$$

represents the articular behavior of the follower robot E.E., whereas

$$\mathbf{M_m}(\mathbf{x_m})\ddot{\mathbf{x}}_{\mathbf{m}} + \mathbf{C_m}(\mathbf{x_m}, \dot{\mathbf{x}}_{\mathbf{m}})\dot{\mathbf{x}}_{\mathbf{m}} + \mathbf{g_m}(\mathbf{x_m}) = \mathbf{f_m} + \mathbf{f_h} \tag{6}$$

represents the Cartesian behavior of the local robot's E.E., where $\mathbf{M_m}$ and $\mathbf{M_s}$ are inertial matrices, $\mathbf{C_m}$ and $\mathbf{C_s}$ are Coriolis and centripetal forces matrices, and $\mathbf{g_m}$ and $\mathbf{g_s}$ are gravitational vectors, for the leader and the follower robots, respectively. Additionally, for the remote robot, $\mathbf{q_s}(t), \dot{\mathbf{q}}_{\mathbf{s}}(t), \ddot{\mathbf{q}}_{\mathbf{s}}(t) \in \mathbb{R}^n$ are the articular position, velocity, and acceleration of the follower, respectively; $\boldsymbol{\tau}_{\mathbf{s}}$ is the control torque applied to the remote robot, and $\mathbf{f_e}$ represents the environment behavior. On the other hand, for the local robot, $\mathbf{x_m}(t), \dot{\mathbf{x}}_{\mathbf{m}}(t), \ddot{\mathbf{x}}_{\mathbf{m}}(t) \in \mathbb{R}^m$ are the Cartesian position, velocity, and acceleration of the leader's E.E., respectively; $\mathbf{f_m}$ is the force applied to the local robot; and $\mathbf{f_h}$ is the force applied by the human operator.

3) CONTROLLERS

In this work, we use Cartesian/articular control schemes [29] based on P+d structures for bilateral teleoperation expressed by

$$\mathbf{f_m} = -k_m\left(\mathbf{ref} - \mathbf{x_s}\left(t - h_2\right)\right) - \alpha_m \dot{\mathbf{x}}_{\mathbf{m}} + \mathbf{g_m} \tag{7}$$

and

$$\boldsymbol{\tau}_{\mathbf{s}} = k_p \mathbf{J}_{\mathbf{D}}^{\dagger}\left(\mathbf{ref}\left(t - h_1\right) - \mathbf{x_s}\right) - \alpha_s \dot{\mathbf{q}}_{\mathbf{s}} + \mathbf{g_s} \tag{8}$$

with $\mathbf{J}_{\mathbf{D}}^{\dagger}$ defined as

$$\mathbf{J}_{\mathbf{D}}^{\dagger} = \mathbf{W}^{-1}\mathbf{J}_{\mathbf{D}}^{\mathbf{T}}\left(\mathbf{J_D}\mathbf{W}^{-1}\mathbf{J}_{\mathbf{D}}^{\mathbf{T}}\right)^{-1}$$

where $\mathbf{J_D} \in \mathbb{R}^{m \times n}$, with n being the degrees of freedom (DoF) of the robot, m being the DoF of the task space, and $\mathbf{W} \in \mathbb{R}^{n \times n}$ is a weighting matrix. The modified Jacobian $\mathbf{J_D}$ depends on $\mathbf{J}$ and is defined in Appendix A.

In this manner, the control objective for the remote robot is to track, with its E.E., the reference produced by the proposed mapping at the local site $\mathbf{ref}(t - h_1)$. Given the structure of (8), the follower robot can be controlled in a coupled way [3]. Therefore, the resulting commands from the controller for the mobile manipulator robot are torques for each joint of the torso-manipulator set and thrust-rotation forces for the mobile platform [13].

The control objective of the delayed bilateral teleoperation is to bound for the stationary state, the coordination error, and the velocities of the leader and follower robots, that is, $\mathbf{e} = \mathbf{ref} - \mathbf{x_s}$, $\dot{\mathbf{x}}_{\mathbf{m}}, \dot{\mathbf{x}}_{\mathbf{s}} \in \mathcal{L}_{\infty}$, despite the time-varying delays.

III. STABILITY ANALYSIS

A. LYAPUNOV–KRASOVSKII CANDIDATE

In this section, we will analyze the stability of the delayed teleoperation system. The proposed Lyapunov–Krasovskii candidate V consists of two parts, namely V_1 and V_2, given by

$$V = V_1 + V_2. \tag{9}$$

First, V_1 is proposed as

$$V_1 = \frac{1}{2}k_1 \mathbf{e}^{\mathbf{T}}\mathbf{e} + \frac{1}{2}k_2 \dot{\mathbf{x}}_{\mathbf{m}}^{\mathbf{T}}\mathbf{M_m}\dot{\mathbf{x}}_{\mathbf{m}} + 2k_4 \mathbf{e}^{\mathbf{T}}\mathbf{M_m}\dot{\mathbf{x}}_{\mathbf{m}} + k_2 E_h + 2\int_{-\bar{h}_2}^{0}\int_{t+\theta}^{t} \dot{\mathbf{x}}_{\mathbf{s}}^{\mathbf{T}}(\rho)\dot{\mathbf{x}}_{\mathbf{s}}(\rho)\, d\rho d\theta \tag{10}$$

which includes the behavior of coordination errors $\mathbf{e}$ and its dynamics $\dot{\mathbf{e}}$ between the local and remote robots

$$\mathbf{e} = \mathbf{ref} - \mathbf{x_s} \tag{11}$$

$$\dot{\mathbf{e}} = \mathbf{r\dot{e}f} - \dot{\mathbf{x}}_{\mathbf{s}} \tag{12}$$

considering the kinetic energy of the leader robot $\dot{\mathbf{x}}_{\mathbf{m}}^{\mathbf{T}}\mathbf{M_m}\dot{\mathbf{x}}_{\mathbf{m}}$, the energy of the human operator E_h, terms related to the energy accumulated in the communication channel, and the term $\mathbf{e}^{\mathbf{T}}\mathbf{M_m}\dot{\mathbf{x}}_{\mathbf{m}}$, which relates the coordination errors and the velocities of the local robot.

The second part of the proposed candidate is

$$V_2 = \frac{1}{2}k_3 \dot{\mathbf{q}}_{\mathbf{s}}^{\mathbf{T}}\mathbf{J}_{\mathbf{D}}^{\mathbf{T}}\mathbf{J_D}\mathbf{M_s}\dot{\mathbf{q}}_s + k_3 E_e + \frac{\eta}{\gamma}\int_{t-\gamma}^{t} \dot{\mathbf{q}}_{\mathbf{s}}^{\mathbf{T}}\mathbf{J}_{\mathbf{D}}^{\mathbf{T}}\mathbf{J_D}\dot{\mathbf{q}}_s + \int_{-\bar{h}_1}^{0}\int_{t+\theta}^{t} \dot{\mathbf{x}}_{\mathbf{m}}^{\mathbf{T}}(\rho)\dot{\mathbf{x}}_{\mathbf{m}}(\rho)\, d\rho d\theta \tag{13}$$

which includes the kinetic energy of the follower robot with $\mathbf{J_D}$ being a modified Jacobian (as shown in Appendix A), the environment energy, and terms related to the energy accumulated by the communication channel.

The positiveness of both V_1 and V_2 is demonstrated in Appendix B.

B. STABILITY ANALYSIS BASED ON LYAPUNOV–KRASOVSKII

In this section, the time derivative of V will be performed and evaluated on the system trajectories.

1) DERIVATIVE OF V_1

Taking (10), the evolution of $\dot{V}_1$ along the trajectories of the system is established as

$$\begin{aligned}\dot{V}_1 = {} & k_1\mathbf{e}^{\mathbf{T}}\dot{\mathbf{e}} + \frac{1}{2}k_2\dot{\mathbf{x}}_{\mathbf{m}}^{\mathbf{T}}\dot{\mathbf{M}}_{\mathbf{m}}\dot{\mathbf{x}}_{\mathbf{m}} + k_2\dot{\mathbf{x}}_{\mathbf{m}}^{\mathbf{T}}\mathbf{M}_{\mathbf{m}}\ddot{\mathbf{x}}_{\mathbf{m}} \\ & + 2k_4\dot{\mathbf{e}}^{\mathbf{T}}\mathbf{M}_{\mathbf{m}}\dot{\mathbf{x}}_{\mathbf{m}} + 2k_4\mathbf{e}^{\mathbf{T}}\mathbf{M}_{\mathbf{m}}\ddot{\mathbf{x}}_{\mathbf{m}} + 2k_4\mathbf{e}^{\mathbf{T}}\dot{\mathbf{M}}_{\mathbf{m}}\dot{\mathbf{x}}_{\mathbf{m}} \\ & + k_2\dot{E}_h + 2\bar{h}_2\dot{\mathbf{x}}_{\mathbf{s}}^{\mathbf{T}}\dot{\mathbf{x}}_{\mathbf{s}} - 2\int_{t-\bar{h}_2}^{t}\dot{\mathbf{x}}_{\mathbf{s}}^{\mathbf{T}}(\rho)\dot{\mathbf{x}}_{\mathbf{s}}(\rho)\,d\rho. \end{aligned} \tag{14}$$

Now, if we include (12) in (14), the mathematical representation of the leader robot from (6), and the proposed controller in (7), using the distributive property of the sum, it yields

$$\begin{aligned}\dot{V}_1 = {} & k_1\mathbf{e}^{\mathbf{T}}\dot{\mathbf{ref}} - k_1\mathbf{e}^{\mathbf{T}}\dot{\mathbf{x}}_{\mathbf{s}} + \frac{1}{2}k_2\dot{\mathbf{x}}_{\mathbf{m}}^{\mathbf{T}}\dot{\mathbf{M}}_{\mathbf{m}}\dot{\mathbf{x}}_{\mathbf{m}} \\ & - \alpha_m k_2\dot{\mathbf{x}}_{\mathbf{m}}^{\mathbf{T}}\dot{\mathbf{x}}_{\mathbf{m}} - k_m k_2\dot{\mathbf{x}}_{\mathbf{m}}^{\mathbf{T}}(\mathbf{ref} - \mathbf{x}_{\mathbf{s}}(t-h_2)) \\ & - k_2\dot{\mathbf{x}}_{\mathbf{m}}^{\mathbf{T}}\mathbf{C}_{\mathbf{m}}\dot{\mathbf{x}}_{\mathbf{m}} + 2k_4\dot{\mathbf{e}}^{\mathbf{T}}\mathbf{M}_{\mathbf{m}}\dot{\mathbf{x}}_{\mathbf{m}} - 2\alpha_m k_4\mathbf{e}^{\mathbf{T}}\dot{\mathbf{x}}_{\mathbf{m}} \\ & - 2k_m k_4\mathbf{e}^{\mathbf{T}}(\mathbf{ref} - \mathbf{x}_{\mathbf{s}}(t-h_2)) - 2k_4\mathbf{e}^{\mathbf{T}}\mathbf{C}_{\mathbf{m}}\dot{\mathbf{x}}_{\mathbf{m}} \\ & + k_2\dot{\mathbf{x}}_{\mathbf{m}}^{\mathbf{T}}\mathbf{f}_{\mathbf{h}} + 2k_4\mathbf{e}^{\mathbf{T}}\mathbf{f}_{\mathbf{h}} + 2k_4\mathbf{e}^{\mathbf{T}}\dot{\mathbf{M}}_{\mathbf{m}}\dot{\mathbf{x}}_{\mathbf{m}} + k_2\dot{E}_h \\ & + 2\bar{h}_2\dot{\mathbf{x}}_{\mathbf{s}}^{\mathbf{T}}\dot{\mathbf{x}}_{\mathbf{s}} - 2\int_{t-\bar{h}_2}^{t}\dot{\mathbf{x}}_{\mathbf{s}}^{\mathbf{T}}(\rho)\dot{\mathbf{x}}_{\mathbf{s}}(\rho)\,d\rho. \end{aligned} \tag{15}$$

The terms $\frac{1}{2}k_2\dot{\mathbf{x}}_{\mathbf{m}}^{\mathbf{T}}\dot{\mathbf{M}}_{\mathbf{m}}\dot{\mathbf{x}}_{\mathbf{m}}$ and $-k_2\dot{\mathbf{x}}_{\mathbf{m}}^{\mathbf{T}}\mathbf{C}_{\mathbf{m}}\dot{\mathbf{x}}_{\mathbf{m}}$ simplify by Property 2 while $k_2\dot{\mathbf{x}}_{\mathbf{m}}^{\mathbf{T}}\mathbf{f}_{\mathbf{h}}$ cancels out with the derivative of k_2E_h. Now, by adding and subtracting $\mathbf{x}_{\mathbf{s}}$ in a couple of terms in (15), considering that $\dot{\mathbf{M}}_{\mathbf{m}} = \mathbf{C}_{\mathbf{m}}^{\mathbf{T}} + \mathbf{C}_{\mathbf{m}}$, knowing that $\int_{t-h}^{t}\dot{\mathbf{x}}(\epsilon)d\epsilon = \mathbf{x}(t) - \mathbf{x}(t-h)$, and using (11), (15) is equal to

$$\begin{aligned}\dot{V}_1 = {} & k_1\mathbf{e}^{\mathbf{T}}\dot{\mathbf{ref}} - k_1\mathbf{e}^{\mathbf{T}}\dot{\mathbf{x}}_{\mathbf{s}} - \alpha_m k_2\dot{\mathbf{x}}_{\mathbf{m}}^{\mathbf{T}}\dot{\mathbf{x}}_{\mathbf{m}} - k_m k_2\dot{\mathbf{x}}_{\mathbf{m}}^{\mathbf{T}}\mathbf{e} \\ & - k_m k_2\dot{\mathbf{x}}_{\mathbf{m}}^{\mathbf{T}}\int_{t-h_2}^{t}\dot{\mathbf{x}}_{\mathbf{s}}(\rho)\,d\rho + 2k_4\dot{\mathbf{e}}^{\mathbf{T}}\mathbf{M}_{\mathbf{m}}\dot{\mathbf{x}}_{\mathbf{m}} \\ & - 2\alpha_m k_4\mathbf{e}^{\mathbf{T}}\dot{\mathbf{x}}_{\mathbf{m}} - 2k_m k_4\mathbf{e}^{\mathbf{T}}\mathbf{e} \\ & - 2k_m k_4\mathbf{e}^{\mathbf{T}}\int_{t-h_2}^{t}\dot{\mathbf{x}}_{\mathbf{s}}(\rho)\,d\rho + 2k_4\mathbf{e}^{\mathbf{T}}\mathbf{f}_{\mathbf{h}} \\ & + 2k_4\mathbf{e}^{\mathbf{T}}\mathbf{C}_{\mathbf{m}}\dot{\mathbf{x}}_{\mathbf{m}} + 2\bar{h}_2\dot{\mathbf{x}}_{\mathbf{s}}^{\mathbf{T}}\dot{\mathbf{x}}_{\mathbf{s}} - 2\int_{t-\bar{h}_2}^{t}\dot{\mathbf{x}}_{\mathbf{s}}^{\mathbf{T}}(\rho)\dot{\mathbf{x}}_{\mathbf{s}}(\rho)\,d\rho. \end{aligned} \tag{16}$$

Rearranging (16), including (4), and using the distributive property of the sum, $\dot{V}_1$ can be rewritten as

$$\begin{aligned}\dot{V}_1 \leqslant {} & -\alpha_m k_2\dot{\mathbf{x}}_{\mathbf{m}}^{\mathbf{T}}\dot{\mathbf{x}}_{\mathbf{m}} - 2k_m k_4\mathbf{e}^{\mathbf{T}}\mathbf{e} + k_1\xi\mathbf{e}^{\mathbf{T}}\boldsymbol{\gamma} \\ & + k_1k_a\varepsilon\mathbf{e}^{\mathbf{T}}\tanh(k_b\mathbf{x}_{\mathbf{m}}) + k_1k_g\beta\mathbf{e}^{\mathbf{T}}\nabla_{\mathbf{fp}}\dot{\mathbf{x}}_{\mathbf{m}} \\ & - k_1\mathbf{e}^{\mathbf{T}}\dot{\mathbf{x}}_{\mathbf{s}} - k_m k_2\dot{\mathbf{x}}_{\mathbf{m}}^{\mathbf{T}}\int_{t-h_2}^{t}\dot{\mathbf{x}}_{\mathbf{s}}(\rho)\,d\rho \\ & - 2k_m k_4\mathbf{e}^{\mathbf{T}}\int_{t-h_2}^{t}\dot{\mathbf{x}}_{\mathbf{s}}(\rho)\,d\rho + 2k_4\dot{\mathbf{e}}^{\mathbf{T}}\mathbf{M}_{\mathbf{m}}\dot{\mathbf{x}}_{\mathbf{m}} \\ & - k_m k_2\dot{\mathbf{x}}_{\mathbf{m}}^{\mathbf{T}}\mathbf{e} - 2\alpha_m k_4\mathbf{e}^{\mathbf{T}}\dot{\mathbf{x}}_{\mathbf{m}} + 2k_4\mathbf{e}^{\mathbf{T}}\mathbf{C}_{\mathbf{m}}\dot{\mathbf{x}}_{\mathbf{m}} \\ & + 2k_4\mathbf{e}^{\mathbf{T}}\mathbf{f}_{\mathbf{h}} + 2\bar{h}_2\dot{\mathbf{x}}_{\mathbf{s}}^{\mathbf{T}}\dot{\mathbf{x}}_{\mathbf{s}} - 2\int_{t-\bar{h}_2}^{t}\dot{\mathbf{x}}_{\mathbf{s}}^{\mathbf{T}}(\rho)\dot{\mathbf{x}}_{\mathbf{s}}(\rho)\,d\rho. \end{aligned} \tag{17}$$

To simplify the bound of $\dot{V}_1$, knowing that $\tanh(k_b\mathbf{x}_{\mathbf{m}}) \leqslant 1$, defining $k_4 = \frac{1}{4}\frac{1}{\alpha_m}$, $k_1 = \frac{1}{k_g}$, $k_2 = \frac{1}{2}\frac{1}{k_m}$ and rearranging (17), we have

$$\begin{aligned}\dot{V}_1 \leqslant {} & -\frac{1}{2}\frac{\alpha_m}{k_m}\dot{\mathbf{x}}_{\mathbf{m}}^{\mathbf{T}}\dot{\mathbf{x}}_{\mathbf{m}} - \frac{1}{2}\frac{k_m}{\alpha_m}\mathbf{e}^{\mathbf{T}}\mathbf{e} + \frac{\xi}{k_g}\mathbf{e}^{\mathbf{T}}\boldsymbol{\gamma} \\ & + \frac{k_a}{k_g}\varepsilon\|\mathbf{e}\| + \beta\mathbf{e}^{\mathbf{T}}\nabla_{\mathbf{fp}}\dot{\mathbf{x}}_{\mathbf{m}} - \frac{1}{2}\dot{\mathbf{x}}_{\mathbf{m}}^{\mathbf{T}}\mathbf{e} - \frac{1}{k_g}\mathbf{e}^{\mathbf{T}}\dot{\mathbf{x}}_{\mathbf{s}} \\ & - \frac{1}{2}\dot{\mathbf{x}}_{\mathbf{m}}^{\mathbf{T}}\int_{t-h_2}^{t}\dot{\mathbf{x}}_{\mathbf{s}}(\rho)\,d\rho - \int_{t-\bar{h}_2}^{t}\dot{\mathbf{x}}_{\mathbf{s}}^{\mathbf{T}}(\rho)\dot{\mathbf{x}}_{\mathbf{s}}(\rho)\,d\rho \\ & - \frac{1}{2}\frac{k_m}{\alpha_m}\mathbf{e}^{\mathbf{T}}\int_{t-h_2}^{t}\dot{\mathbf{x}}_{\mathbf{s}}(\rho)\,d\rho - \int_{t-\bar{h}_2}^{t}\dot{\mathbf{x}}_{\mathbf{s}}^{\mathbf{T}}(\rho)\dot{\mathbf{x}}_{\mathbf{s}}(\rho)\,d\rho \\ & + \frac{1}{2}\frac{1}{\alpha_m}\dot{\mathbf{e}}^{\mathbf{T}}\mathbf{M}_{\mathbf{m}}\dot{\mathbf{x}}_{\mathbf{m}} - \frac{1}{2}\mathbf{e}^{\mathbf{T}}\dot{\mathbf{x}}_{\mathbf{m}} + \frac{1}{2}\frac{1}{\alpha_m}\mathbf{e}^{\mathbf{T}}\mathbf{C}_{\mathbf{m}}\dot{\mathbf{x}}_{\mathbf{m}} \\ & + \frac{1}{2}\frac{1}{\alpha_m}\mathbf{e}^{\mathbf{T}}\mathbf{f}_{\mathbf{h}} + 2\bar{h}_2\dot{\mathbf{x}}_{\mathbf{s}}^{\mathbf{T}}\dot{\mathbf{x}}_{\mathbf{s}}. \end{aligned} \tag{18}$$

Taking into account Lemma 1, it can be established that the eighth and ninth term of (18) hold

$$\begin{aligned} & -\frac{1}{2}\dot{\mathbf{x}}_{\mathbf{m}}^{\mathbf{T}}\int_{t-h_2}^{t}\dot{\mathbf{x}}_{\mathbf{s}}(\rho)\,d\rho - \int_{t-\bar{h}_2}^{t}\dot{\mathbf{x}}_{\mathbf{s}}^{\mathbf{T}}(\rho)\dot{\mathbf{x}}_{\mathbf{s}}(\rho)\,d\rho \\ & \leqslant \frac{1}{16}\bar{h}_2\dot{\mathbf{x}}_{\mathbf{m}}^{\mathbf{T}}\dot{\mathbf{x}}_{\mathbf{m}} \end{aligned} \tag{19}$$

while the tenth and eleventh term of (18) verify

$$\begin{aligned} & -\frac{1}{2}\frac{k_m}{\alpha_m}\mathbf{e}^{\mathbf{T}}\int_{t-h_2}^{t}\dot{\mathbf{x}}_{\mathbf{s}}(\rho)\,d\rho - \int_{t-\bar{h}_2}^{t}\dot{\mathbf{x}}_{\mathbf{s}}^{\mathbf{T}}(\rho)\dot{\mathbf{x}}_{\mathbf{s}}(\rho)\,d\rho \\ & \leqslant \frac{\bar{h}_2}{16}\frac{k_m^2}{\alpha_m^2}\mathbf{e}^{\mathbf{T}}\mathbf{e}. \end{aligned} \tag{20}$$

Now, replacing (12), (19), and (20) into (18), using again $\dot{\mathbf{ref}} \leqslant \xi\boldsymbol{\gamma} + \varepsilon k_a\tanh(k_b\mathbf{x}_{\mathbf{m}}) + \beta k_g\nabla_{\mathbf{fp}}\dot{\mathbf{x}}_{\mathbf{m}}$, considering Property 3, using the distributive property to extend the terms added when replacing $\dot{\mathbf{ref}}$, and employing the associative property to group terms related to $\mathbf{e}^{\mathbf{T}}\dot{\mathbf{x}}_{\mathbf{m}}$, $\dot{V}_1$ of (18) results in

$$\begin{aligned}\dot{V}_1 \leqslant {} & -\frac{1}{2}\frac{\alpha_m}{k_m}\dot{\mathbf{x}}_{\mathbf{m}}^{\mathbf{T}}\dot{\mathbf{x}}_{\mathbf{m}} - \frac{1}{2}\frac{k_m}{\alpha_m}\mathbf{e}^{\mathbf{T}}\mathbf{e} + 2\bar{h}_2\dot{\mathbf{x}}_{\mathbf{s}}^{\mathbf{T}}\dot{\mathbf{x}}_{\mathbf{s}} \\ & + \frac{1}{16}\bar{h}_2\dot{\mathbf{x}}_{\mathbf{m}}^{\mathbf{T}}\dot{\mathbf{x}}_{\mathbf{m}} + \frac{1}{16}\frac{k_m^2\bar{h}_2}{\alpha_m^2}\mathbf{e}^{\mathbf{T}}\mathbf{e} + \mathbf{e}^{\mathbf{T}}\left(\beta\nabla_{\mathbf{fp}} - \mathbf{I}\right)\dot{\mathbf{x}}_{\mathbf{m}} \\ & + \frac{1}{2}\frac{\xi}{\alpha_m}\boldsymbol{\gamma}^{\mathbf{T}}\mathbf{M}_{\mathbf{m}}\dot{\mathbf{x}}_{\mathbf{m}} + \frac{1}{2}\frac{k_a}{\alpha_m}\varepsilon\tanh(k_b\mathbf{x}_{\mathbf{m}})^{\mathbf{T}}\mathbf{M}_{\mathbf{m}}\dot{\mathbf{x}}_{\mathbf{m}} \\ & + \frac{1}{2}\frac{k_g}{\alpha_m}\beta\dot{\mathbf{x}}_{\mathbf{m}}^{\mathbf{T}}\nabla_{\mathbf{fp}}^{\mathbf{T}}\mathbf{M}_{\mathbf{m}}\dot{\mathbf{x}}_{\mathbf{m}} - \frac{1}{k_g}\mathbf{e}^{\mathbf{T}}\dot{\mathbf{x}}_{\mathbf{s}} \\ & - \frac{1}{2}\frac{1}{\alpha_m}\dot{\mathbf{x}}_{\mathbf{s}}^{\mathbf{T}}\mathbf{M}_{\mathbf{m}}\dot{\mathbf{x}}_{\mathbf{m}} + \frac{1}{2}\frac{\chi}{\alpha_m}\|\mathbf{e}\|\dot{\mathbf{x}}_{\mathbf{m}}^{\mathbf{T}}\dot{\mathbf{x}}_{\mathbf{m}} + \frac{\xi}{k_g}\mathbf{e}^{\mathbf{T}}\boldsymbol{\gamma} \end{aligned}$$

$$+\frac{k_a}{k_g}\varepsilon\,\|\mathbf{e}\|+\frac{1}{2}\frac{1}{\alpha_m}\mathbf{e}^{\mathbf{T}}\mathbf{f_h}. \tag{21}$$

Moreover, the eleventh term of (21) holds

$$\begin{aligned}&-\frac{1}{2}\frac{1}{\alpha_m}\dot{\mathbf{x}}_{\mathbf{s}}^{\mathbf{T}}\mathbf{M_m}\dot{\mathbf{x}}_{\mathbf{m}}\\&\leqslant\frac{1}{4}\frac{1}{\alpha_m}\dot{\mathbf{x}}_{\mathbf{s}}^{\mathbf{T}}\dot{\mathbf{x}}_{\mathbf{s}}+\frac{1}{4}\frac{1}{\alpha_m}\dot{\mathbf{x}}_{\mathbf{m}}^{\mathbf{T}}\mathbf{M}_{\mathbf{m}}^{\mathbf{T}}\mathbf{M_m}\dot{\mathbf{x}}_{\mathbf{m}}.\end{aligned} \tag{22}$$

Now, (22) is replaced in (21), and considering the most unfavorable case for the crossed terms except $-\frac{1}{k_g}\mathbf{e}^{\mathbf{T}}\dot{\mathbf{x}}_{\mathbf{s}}$, we have

$$\begin{aligned}\dot{V}_1\leqslant&-\frac{1}{2}\frac{\alpha_m}{k_m}\dot{\mathbf{x}}_{\mathbf{m}}^{\mathbf{T}}\dot{\mathbf{x}}_{\mathbf{m}}-\frac{1}{2}\frac{k_m}{\alpha_m}\mathbf{e}^{\mathbf{T}}\mathbf{e}+2\bar{h}_2\dot{\mathbf{x}}_{\mathbf{s}}^{\mathbf{T}}\dot{\mathbf{x}}_{\mathbf{s}}\\&+\frac{1}{16}\bar{h}_2\dot{\mathbf{x}}_{\mathbf{m}}^{\mathbf{T}}\dot{\mathbf{x}}_{\mathbf{m}}+\frac{1}{16}\frac{\bar{h}_2k_m^2}{\alpha_m^2}\mathbf{e}^{\mathbf{T}}\mathbf{e}\\&+\frac{1}{2}\frac{k_g}{\alpha_m}\beta\dot{\mathbf{x}}_{\mathbf{m}}^{\mathbf{T}}\nabla_{\mathbf{fp}}\mathbf{M_m}\dot{\mathbf{x}}_{\mathbf{m}}+\frac{1}{4}\frac{1}{\alpha_m}\dot{\mathbf{x}}_{\mathbf{s}}^{\mathbf{T}}\dot{\mathbf{x}}_{\mathbf{s}}\\&+\frac{1}{4}\frac{1}{\alpha_m}\dot{\mathbf{x}}_{\mathbf{m}}^{\mathbf{T}}\mathbf{M}_{\mathbf{m}}^{\mathbf{T}}\mathbf{M_m}\dot{\mathbf{x}}_{\mathbf{m}}+\|\mathbf{e}\|\|\beta\nabla_{\mathbf{fp}}-\mathbf{I}\|\|\dot{\mathbf{x}}_{\mathbf{m}}\|\\&-\frac{1}{k_g}\mathbf{e}^{\mathbf{T}}\dot{\mathbf{x}}_{\mathbf{s}}+\frac{1}{2}\frac{\chi}{\alpha_m}\|\mathbf{e}\|\,\dot{\mathbf{x}}_{\mathbf{m}}^{\mathbf{T}}\dot{\mathbf{x}}_{\mathbf{m}}\\&+\frac{\xi}{k_g}\|\mathbf{e}\|\,\|\boldsymbol{\gamma}\|+\frac{k_a}{k_g}\varepsilon\,\|\mathbf{e}\|+\frac{1}{\alpha_m}\|\mathbf{e}\|\,\|\mathbf{f_h}\|\\&+\frac{1}{2}\frac{\xi}{\alpha_m}\|\boldsymbol{\gamma}\|\,\|\mathbf{M_m}\|\,\|\dot{\mathbf{x}}_{\mathbf{m}}\|+\frac{1}{2}\frac{k_a}{\alpha_m}\varepsilon\,\|\mathbf{M_m}\|\,\|\dot{\mathbf{x}}_{\mathbf{m}}\|.\end{aligned} \tag{23}$$

Now, taking into account that $\dot{\mathbf{x}}_{\mathbf{s}}=\mathbf{J}\dot{\mathbf{q}}_{\mathbf{s}}$, then $\frac{1}{k_g}\mathbf{e}^{\mathbf{T}}\dot{\mathbf{x}}_{\mathbf{s}}=\frac{1}{k_g}\dot{\mathbf{q}}_{\mathbf{s}}^{\mathbf{T}}\mathbf{J}^{\mathbf{T}}\mathbf{e}$. In addition, we can use the associative property of addition for the third and seventh terms of (23), having

$$\dot{\mathbf{x}}_{\mathbf{s}}^{\mathbf{T}}\left[2\bar{h}_2\mathbf{I}+\frac{1}{4}\frac{1}{\alpha_m}\right]\dot{\mathbf{x}}_{\mathbf{s}}=\dot{\mathbf{q}}_{\mathbf{s}}^{\mathbf{T}}\left[2\bar{h}_2\mathbf{J}^{\mathbf{T}}\mathbf{J}+\frac{1}{4}\frac{1}{\alpha_m}\mathbf{J}^{\mathbf{T}}\mathbf{J}\right]\dot{\mathbf{q}}_{\mathbf{s}}. \tag{24}$$

Replacing (24) into (23) and using Property 1, $\dot{V}_1$ is established as

$$\begin{aligned}\dot{V}_1\leqslant&-\frac{1}{2}\frac{\alpha_m}{k_m}\dot{\mathbf{x}}_{\mathbf{m}}^{\mathbf{T}}\dot{\mathbf{x}}_{\mathbf{m}}-\frac{1}{2}\frac{k_m}{\alpha_m}\mathbf{e}^{\mathbf{T}}\mathbf{e}\\&+\dot{\mathbf{q}}_{\mathbf{s}}^{\mathbf{T}}\left[2\bar{h}_2\mathbf{J}^{\mathbf{T}}\mathbf{J}+\frac{1}{4}\frac{1}{\alpha_m}\mathbf{J}^{\mathbf{T}}\mathbf{J}\right]\dot{\mathbf{q}}_{\mathbf{s}}+\frac{1}{16}\bar{h}_2\dot{\mathbf{x}}_{\mathbf{m}}^{\mathbf{T}}\dot{\mathbf{x}}_{\mathbf{m}}\\&+\frac{1}{16}\frac{\bar{h}_2k_m^2}{\alpha_m^2}\mathbf{e}^{\mathbf{T}}\mathbf{e}+\frac{1}{2}\frac{k_g}{\alpha_m}\beta\dot{\mathbf{x}}_{\mathbf{m}}^{\mathbf{T}}\nabla_{\mathbf{fp}}\mathbf{M_m}\dot{\mathbf{x}}_{\mathbf{m}}\\&+\frac{1}{4}\frac{1}{\alpha_m}\dot{\mathbf{x}}_{\mathbf{m}}^{\mathbf{T}}\mathbf{M}_{\mathbf{m}}^{\mathbf{T}}\mathbf{M_m}\dot{\mathbf{x}}_{\mathbf{m}}+\|\mathbf{e}\|\|\beta\nabla_{\mathbf{fp}}-\mathbf{I}\|\|\dot{\mathbf{x}}_{\mathbf{m}}\|\\&-\frac{1}{k_g}\dot{\mathbf{q}}_{\mathbf{s}}^{\mathbf{T}}\mathbf{J}^{\mathbf{T}}\mathbf{e}+\frac{1}{2}\frac{\chi}{\alpha_m}\|\mathbf{e}\|\,\dot{\mathbf{x}}_{\mathbf{m}}^{\mathbf{T}}\dot{\mathbf{x}}_{\mathbf{m}}+\frac{\xi}{k_g}\|\mathbf{e}\|\,\|\boldsymbol{\gamma}\|\\&+\frac{k_a}{k_g}\varepsilon\,\|\mathbf{e}\|+\frac{1}{2}\frac{1}{\alpha_m}\|\mathbf{e}\|\,\|\mathbf{f_h}\|+\frac{1}{2}\frac{\xi}{\alpha_m}\lambda_{m_{max}}\|\boldsymbol{\gamma}\|\,\|\dot{\mathbf{x}}_{\mathbf{m}}\|\\&+\frac{1}{2}\frac{k_a}{\alpha_m}\varepsilon\lambda_{m_{max}}\|\dot{\mathbf{x}}_{\mathbf{m}}\|.\end{aligned} \tag{25}$$

2) DERIVATIVE OF V_2

The evolution of $\dot{V}_2$ along the trajectories of the system is established as

$$\begin{aligned}\dot{V}_2=&\,k_3\dot{\mathbf{q}}_{\mathbf{s}}^{\mathbf{T}}\mathbf{J}_{\mathbf{D}}^{\mathbf{T}}\mathbf{J_D}\mathbf{M_s}\ddot{\mathbf{q}}_{\mathbf{s}}+\frac{1}{2}k_3\dot{\mathbf{q}}_{\mathbf{s}}^{\mathbf{T}}\mathbf{J_D}^{\mathbf{T}}\mathbf{J_D}\dot{\mathbf{M}}_{\mathbf{s}}\dot{\mathbf{q}}_{\mathbf{s}}\\&+\frac{1}{2}k_3\dot{\mathbf{q}}_{\mathbf{s}}^{\mathbf{T}}(\dot{\mathbf{J}}_{\mathbf{D}}^{\mathbf{T}}\mathbf{J_D}+\mathbf{J}_{\mathbf{D}}^{\mathbf{T}}\dot{\mathbf{J}}_{\mathbf{D}})\mathbf{M_s}\dot{\mathbf{q}}_{\mathbf{s}}+k_3\dot{E}_e\\&+\bar{h}_1\dot{\mathbf{x}}_{\mathbf{m}}^{\mathbf{T}}\dot{\mathbf{x}}_{\mathbf{m}}-\int_{t-\bar{h}_1}^{t}\dot{\mathbf{x}}_{\mathbf{m}}^{\mathbf{T}}(\rho)\dot{\mathbf{x}}_{\mathbf{m}}(\rho)\,d\rho\\&+\frac{\eta}{\delta}\dot{\mathbf{q}}_{\mathbf{s}}^{\mathbf{T}}\mathbf{J}_{\mathbf{D}}^{\mathbf{T}}\mathbf{J_D}\dot{\mathbf{q}}_{\mathbf{s}}-\frac{\eta}{\delta}\dot{\mathbf{q}}_{\mathbf{s}}^{\mathbf{T}}(t-\delta)\,\mathbf{J}_{\mathbf{D}}^{\mathbf{T}}\mathbf{J_D}\dot{\mathbf{q}}_{\mathbf{s}}(t-\delta).\end{aligned} \tag{26}$$

Now, considering the dynamics of the follower in joint space given in (5) and the proposed controller (8), we have

$$\begin{aligned}\dot{V}_2=&\,k_3k_p\dot{\mathbf{q}}_{\mathbf{s}}^{\mathbf{T}}\mathbf{J}_{\mathbf{D}}^{\mathbf{T}}\mathbf{J_D}\mathbf{J}_{\mathbf{D}}^{\dagger}\mathbf{e}_1-k_3\alpha_s\dot{\mathbf{q}}_{\mathbf{s}}^{\mathbf{T}}\mathbf{J}_{\mathbf{D}}^{\mathbf{T}}\mathbf{J_D}\dot{\mathbf{q}}_{\mathbf{s}}\\&+k_3\dot{\mathbf{q}}_{\mathbf{s}}^{\mathbf{T}}\mathbf{J}_{\mathbf{D}}^{\mathbf{T}}\mathbf{J_D}\mathbf{J}^{\mathbf{T}}\mathbf{f_e}-k_3\dot{\mathbf{q}}_{\mathbf{s}}^{\mathbf{T}}\mathbf{J}_{\mathbf{D}}^{\mathbf{T}}\mathbf{J_D}\mathbf{C_s}\dot{\mathbf{q}}_{\mathbf{s}}\\&+\frac{1}{2}k_3\dot{\mathbf{q}}_{\mathbf{s}}^{\mathbf{T}}\mathbf{J}_{\mathbf{D}}^{\mathbf{T}}\mathbf{J_D}\dot{\mathbf{M}}_{\mathbf{s}}\dot{\mathbf{q}}_{\mathbf{s}}\\&+\frac{1}{2}k_3\dot{\mathbf{q}}_{\mathbf{s}}^{\mathbf{T}}(\dot{\mathbf{J}}_{\mathbf{D}}^{\mathbf{T}}\mathbf{J_D}+\mathbf{J}_{\mathbf{D}}^{\mathbf{T}}\dot{\mathbf{J}}_{\mathbf{D}})\mathbf{M_s}\dot{\mathbf{q}}_{\mathbf{s}}-k_3\mathbf{f}_{\mathbf{e}}^{\mathbf{T}}\dot{\mathbf{x}}_{\mathbf{s}}\\&+\bar{h}_1\dot{\mathbf{x}}_{\mathbf{m}}^{\mathbf{T}}\dot{\mathbf{x}}_{\mathbf{m}}-\int_{t-\bar{h}_1}^{t}\dot{\mathbf{x}}_{\mathbf{m}}^{\mathbf{T}}(\rho)\dot{\mathbf{x}}_{\mathbf{m}}(\rho)\,d\rho\\&+\frac{\eta}{\delta}\dot{\mathbf{q}}_{\mathbf{s}}^{\mathbf{T}}\mathbf{J}_{\mathbf{D}}^{\mathbf{T}}\mathbf{J_D}\dot{\mathbf{q}}_{\mathbf{s}}-\frac{\eta}{\delta}\dot{\mathbf{q}}_{\mathbf{s}}^{\mathbf{T}}(t-\delta)\,\mathbf{J}_{\mathbf{D}}^{\mathbf{T}}\mathbf{J_D}\dot{\mathbf{q}}_{\mathbf{s}}(t-\delta).\end{aligned} \tag{27}$$

Considering well-known properties of matrix pseudoinverses, then

$$\mathbf{J_D}\mathbf{J}_{\mathbf{D}}^{\dagger}=\mathbf{J_D}\mathbf{W}^{-1}\mathbf{J}_{\mathbf{D}}^{\mathbf{T}}\left(\mathbf{J_D}\mathbf{W}^{-1}\mathbf{J}_{\mathbf{D}}^{\mathbf{T}}\right)^{-1}=\mathbf{I}$$

while if we use Property 2 for the terms $-k_3\dot{\mathbf{q}}_{\mathbf{s}}^{\mathbf{T}}\mathbf{J}_{\mathbf{D}}^{\mathbf{T}}\mathbf{J_D}\mathbf{C_s}\dot{\mathbf{q}}_{\mathbf{s}}$ and $k_3\dot{\mathbf{q}}_{\mathbf{s}}^{\mathbf{T}}\mathbf{J}_{\mathbf{D}}^{\mathbf{T}}\mathbf{J_D}\frac{1}{2}\dot{\mathbf{M}}_{\mathbf{s}}\dot{\mathbf{q}}_{\mathbf{s}}$, and add and subtract rate/NL-position references $\mathbf{ref}$, $\dot{V}_2$ is expressed as

$$\begin{aligned}\dot{V}_2=&\,k_3k_p\dot{\mathbf{q}}_{\mathbf{s}}^{\mathbf{T}}\mathbf{J}_{\mathbf{D}}^{\mathbf{T}}(\mathbf{ref}\,(t-h_1)-\mathbf{x_s}+\mathbf{ref}-\mathbf{ref})\\&-k_3\alpha_s\dot{\mathbf{q}}_{\mathbf{s}}^{\mathbf{T}}\mathbf{J}_{\mathbf{D}}^{\mathbf{T}}\mathbf{J_D}\dot{\mathbf{q}}_{\mathbf{s}}+k_3\dot{\mathbf{q}}_{\mathbf{s}}^{\mathbf{T}}\mathbf{J}_{\mathbf{D}}^{\mathbf{T}}\mathbf{J_D}\mathbf{J}^{\mathbf{T}}\mathbf{f_e}\\&+\frac{1}{2}k_3\dot{\mathbf{q}}_{\mathbf{s}}^{\mathbf{T}}(\dot{\mathbf{J}}_{\mathbf{D}}^{\mathbf{T}}\mathbf{J_D}+\mathbf{J}_{\mathbf{D}}^{\mathbf{T}}\dot{\mathbf{J}}_{\mathbf{D}})\mathbf{M_s}\dot{\mathbf{q}}_{\mathbf{s}}-k_3\mathbf{f}_{\mathbf{e}}^{\mathbf{T}}\dot{\mathbf{x}}_{\mathbf{s}}\\&+\bar{h}_1\dot{\mathbf{x}}_{\mathbf{m}}^{\mathbf{T}}\dot{\mathbf{x}}_{\mathbf{m}}-\int_{t-\bar{h}_1}^{t}\dot{\mathbf{x}}_{\mathbf{m}}^{\mathbf{T}}(\rho)\dot{\mathbf{x}}_{\mathbf{m}}(\rho)\,d\rho\\&+\frac{\eta}{\delta}\dot{\mathbf{q}}_{\mathbf{s}}^{\mathbf{T}}\mathbf{J}_{\mathbf{D}}^{\mathbf{T}}\mathbf{J_D}\dot{\mathbf{q}}_{\mathbf{s}}-\frac{\eta}{\delta}\dot{\mathbf{q}}_{\mathbf{s}}^{\mathbf{T}}(t-\delta)\,\mathbf{J}_{\mathbf{D}}^{\mathbf{T}}\mathbf{J_D}\dot{\mathbf{q}}_{\mathbf{s}}(t-\delta).\end{aligned} \tag{28}$$

Equation (28) can be manipulated to insert the coordination error given in (11), operate it knowing that $\int_{t-h}^{t}\dot{\mathbf{x}}(\epsilon)d\epsilon=\mathbf{x}(t)-\mathbf{x}(t-h)$ to obtain $k_3k_p\dot{\mathbf{q}}_{\mathbf{s}}^{\mathbf{T}}\mathbf{J}_{\mathbf{D}}^{\mathbf{T}}\int_{t-h_1}^{t}\dot{\mathbf{ref}}(\rho)d\rho$, replace $\dot{\mathbf{ref}}$ with (4), and use the distributive property of the sum, resulting in

$$\dot{V}_2=k_3k_p\dot{\mathbf{q}}_{\mathbf{s}}^{\mathbf{T}}\mathbf{J}_{\mathbf{D}}^{\mathbf{T}}\mathbf{e}-k_3k_p\dot{\mathbf{q}}_{\mathbf{s}}^{\mathbf{T}}\mathbf{J}_{\mathbf{D}}^{\mathbf{T}}\int_{t-h_1}^{t}\xi\boldsymbol{\gamma}d\rho$$

$$
\begin{aligned}
&-k_3k_p\dot{\mathbf{q}}_\mathbf{s}^\mathbf{T}\mathbf{J}_\mathbf{D}^\mathbf{T}\int_{t-h_1}^{t}\varepsilon k_a\tanh\left(k_b\mathbf{x_m}\right)d\rho\\
&-k_3k_p\dot{\mathbf{q}}_\mathbf{s}^\mathbf{T}\mathbf{J}_\mathbf{D}^\mathbf{T}\int_{t-h_1}^{t}\beta k_g\nabla_\mathbf{fp}\dot{\mathbf{x}}_\mathbf{m}d\rho\\
&-k_3\alpha_s\dot{\mathbf{q}}_\mathbf{s}^\mathbf{T}\mathbf{J}_\mathbf{D}^\mathbf{T}\mathbf{J_D}\dot{\mathbf{q}}_\mathbf{s}+k_3\dot{\mathbf{q}}_\mathbf{s}^\mathbf{T}\mathbf{J}_\mathbf{D}^\mathbf{T}\mathbf{J_D}\mathbf{J}^\mathbf{T}\mathbf{f_e}\\
&+\frac{1}{2}k_3\dot{\mathbf{q}}_\mathbf{s}^\mathbf{T}(\dot{\mathbf{J}}_\mathbf{D}^\mathbf{T}\mathbf{J_D}+\mathbf{J}_\mathbf{D}^\mathbf{T}\dot{\mathbf{J}}_\mathbf{D})\mathbf{M_s}\dot{\mathbf{q}}_\mathbf{s}-k_3\mathbf{f}_\mathbf{e}^\mathbf{T}\dot{\mathbf{x}}_\mathbf{s}\\
&+\bar{h}_1\dot{\mathbf{x}}_\mathbf{m}^\mathbf{T}\dot{\mathbf{x}}_\mathbf{m}-\int_{t-\bar{h}_1}^{t}\dot{\mathbf{x}}_\mathbf{m}^\mathbf{T}(\rho)\dot{\mathbf{x}}_\mathbf{m}\left(\rho\right)d\rho\\
&+\frac{\eta}{\delta}\dot{\mathbf{q}}_\mathbf{s}^\mathbf{T}\mathbf{J}_\mathbf{D}^\mathbf{T}\mathbf{J_D}\dot{\mathbf{q}}_\mathbf{s}-\frac{\eta}{\delta}\dot{\mathbf{q}}_\mathbf{s}^\mathbf{T}\left(t-\delta\right)\mathbf{J}_\mathbf{D}^\mathbf{T}\mathbf{J_D}\dot{\mathbf{q}}_\mathbf{s}\left(t-\delta\right).
\end{aligned}
\tag{29}
$$

To simplify the bound of $\dot{V}_2$, we have that $\int_{t-h_1}^{t}d\rho\leqslant\bar{h}_1$, $\tanh(k_b\mathbf{x_m})\leqslant 1$, $\int_{t-h_1}^{t}\tanh(k_b\mathbf{x_m}(\rho))d\rho\leqslant\bar{h}_1$, $\int_{t-h_1}^{t}\nabla_\mathbf{fp}\dot{\mathbf{x}}_\mathbf{m}\,d\rho\leqslant\bar{\nabla}_\mathbf{fp}\int_{t-h_1}^{t}\|\dot{\mathbf{x}}_\mathbf{m}\|d\rho$, where $\bar{\nabla}_\mathbf{fp}$ is the upper bound of $\nabla_\mathbf{fp}$, i.e., $\nabla_\mathbf{fp}\leqslant\bar{\nabla}_\mathbf{fp}$. Moreover, having $\dot{\mathbf{x}}_\mathbf{s}=\mathbf{J}\dot{\mathbf{q}}_\mathbf{s}$, using the distributive property of addition, and considering the most unfavorable case for the crossed terms, $\dot{V}_2$ of (29) results in

$$
\begin{aligned}
\dot{V}_2\leq\;&k_3k_p\dot{\mathbf{q}}_\mathbf{s}^\mathbf{T}\mathbf{J}_\mathbf{D}^\mathbf{T}\mathbf{e}+k_3k_p\xi\bar{h}_1\|\dot{\mathbf{q}}_\mathbf{s}\|\,\|\mathbf{J_D}\|\,\|\boldsymbol{\gamma}\|\\
&+k_3k_ak_p\bar{h}_1\varepsilon\|\dot{\mathbf{q}}_\mathbf{s}\|\,\|\mathbf{J_D}\|+\bar{h}_1\dot{\mathbf{x}}_\mathbf{m}^\mathbf{T}\dot{\mathbf{x}}_\mathbf{m}\\
&-k_3k_gk_p\beta\dot{\mathbf{q}}_\mathbf{s}^\mathbf{T}\mathbf{J}_\mathbf{D}^\mathbf{T}\bar{\nabla}_\mathbf{fp}\int_{t-h_1}^{t}\|\dot{\mathbf{x}}_\mathbf{m}\|\,d\rho\\
&-\int_{t-\bar{h}_1}^{t}\dot{\mathbf{x}}_\mathbf{m}^\mathbf{T}(\rho)\dot{\mathbf{x}}_\mathbf{m}\left(\rho\right)d\rho-k_3\alpha_s\dot{\mathbf{q}}_\mathbf{s}^\mathbf{T}\mathbf{J}_\mathbf{D}^\mathbf{T}\mathbf{J_D}\dot{\mathbf{q}}_\mathbf{s}\\
&-k_3\dot{\mathbf{q}}_\mathbf{s}^\mathbf{T}\left(\mathbf{I}-\mathbf{J}_\mathbf{D}^\mathbf{T}\mathbf{J_D}\right)\mathbf{J}^\mathbf{T}\mathbf{f_e}\\
&+\frac{1}{2}k_3\dot{\mathbf{q}}_\mathbf{s}^\mathbf{T}(\dot{\mathbf{J}}_\mathbf{D}^\mathbf{T}\mathbf{J_D}+\mathbf{J}_\mathbf{D}^\mathbf{T}\dot{\mathbf{J}}_\mathbf{D})\mathbf{M_s}\dot{\mathbf{q}}_\mathbf{s}\\
&+\frac{\eta}{\delta}\dot{\mathbf{q}}_\mathbf{s}^\mathbf{T}\mathbf{J}_\mathbf{D}^\mathbf{T}\mathbf{J_D}\dot{\mathbf{q}}_\mathbf{s}-\frac{\eta}{\delta}\dot{\mathbf{q}}_\mathbf{s}^\mathbf{T}\left(t-\delta\right)\mathbf{J}_\mathbf{D}^\mathbf{T}\mathbf{J_D}\dot{\mathbf{q}}_\mathbf{s}\left(t-\delta\right).
\end{aligned}
\tag{30}
$$

Given that $\mathbf{I}-\mathbf{J}_\mathbf{D}^\mathbf{T}(\mathbf{q})\mathbf{J_D}(\mathbf{q})\in\mathbb{R}^{n\times n}$ is a matrix which projects $\mathbf{J}^\mathbf{T}\mathbf{f_e}$ to the null space of $\mathbf{J_D}$; therefore, $(\mathbf{I}-\mathbf{J}_\mathbf{D}^\mathbf{T}\mathbf{J_D})\mathbf{J}^\mathbf{T}\mathbf{f_e}=\mathbf{0}$ [30]. Taking into account Lemma 1, it can be established that the fifth and sixth terms of (30) hold

$$
\begin{aligned}
&-k_3k_gk_p\beta\dot{\mathbf{q}}_\mathbf{s}^\mathbf{T}\mathbf{J}_\mathbf{D}^\mathbf{T}\bar{\nabla}_\mathbf{fp}\int_{t-h_1}^{t}\|\dot{\mathbf{x}}_\mathbf{m}\|\,d\rho\\
&-\int_{t-\bar{h}_1}^{t}\dot{\mathbf{x}}_\mathbf{m}^\mathbf{T}(\rho)\dot{\mathbf{x}}_\mathbf{m}\left(\rho\right)d\rho\\
&\leq\frac{1}{4}\bar{h}_1k_3{}^2k_g{}^2k_p{}^2\beta^2\dot{\mathbf{q}}_\mathbf{s}^\mathbf{T}\mathbf{J}_\mathbf{D}^\mathbf{T}\bar{\nabla}_\mathbf{fp}\bar{\nabla}_\mathbf{fp}^\mathbf{T}\mathbf{J_D}\dot{\mathbf{q}}_\mathbf{s}.
\end{aligned}
\tag{31}
$$

Using (31), considering $k_3=\frac{1}{k_gk_p}$, $\dot{V}_2$ is finally established as

$$
\begin{aligned}
\dot{V}_2\leq\;&\frac{1}{k_g}\dot{\mathbf{q}}_\mathbf{s}^\mathbf{T}\mathbf{J}_\mathbf{D}^\mathbf{T}\mathbf{e}+\frac{\xi\bar{h}_1}{k_g}\|\dot{\mathbf{q}}_\mathbf{s}\|\,\|\mathbf{J_D}\|\,\|\boldsymbol{\gamma}\|\\
&+\frac{k_a\bar{h}_1}{k_g}\varepsilon\|\dot{\mathbf{q}}_\mathbf{s}\|\,\|\mathbf{J_D}\|+\frac{1}{4}\bar{h}_1\beta^2\dot{\mathbf{q}}_\mathbf{s}^\mathbf{T}\mathbf{J}_\mathbf{D}^\mathbf{T}\bar{\nabla}_\mathbf{fp}\bar{\nabla}_\mathbf{fp}^\mathbf{T}\mathbf{J_D}\dot{\mathbf{q}}_\mathbf{s}\\
&-\frac{\alpha_s}{k_gk_p}\dot{\mathbf{q}}_\mathbf{s}^\mathbf{T}\mathbf{J}_\mathbf{D}^\mathbf{T}\mathbf{J_D}\dot{\mathbf{q}}_\mathbf{s}\\
&+\frac{1}{2}\frac{1}{k_gk_p}\dot{\mathbf{q}}_\mathbf{s}^\mathbf{T}(\dot{\mathbf{J}}_\mathbf{D}^\mathbf{T}\mathbf{J_D}+\mathbf{J}_\mathbf{D}^\mathbf{T}\dot{\mathbf{J}}_\mathbf{D})\mathbf{M_s}\dot{\mathbf{q}}_\mathbf{s}+\bar{h}_1\dot{\mathbf{x}}_\mathbf{m}^\mathbf{T}\dot{\mathbf{x}}_\mathbf{m}\\
&+\frac{\eta}{\delta}\dot{\mathbf{q}}_\mathbf{s}^\mathbf{T}\mathbf{J}_\mathbf{D}^\mathbf{T}\mathbf{J_D}\dot{\mathbf{q}}_\mathbf{s}-\frac{\eta}{\delta}\dot{\mathbf{q}}_\mathbf{s}^\mathbf{T}\left(t-\delta\right)\mathbf{J}_\mathbf{D}^\mathbf{T}\mathbf{J_D}\dot{\mathbf{q}}_\mathbf{s}\left(t-\delta\right).
\end{aligned}
\tag{32}
$$

3) ADDITION OF THE CANDIDATE DERIVATIVES

The procedure developed in previous sections allows us to obtain $\dot{V}$ adding $\dot{V}_1$ and $\dot{V}_2$, considering that the ninth term of (25) and the first term of (32) holds

$$
\begin{aligned}
\frac{1}{k_g}\dot{\mathbf{q}}_\mathbf{s}^\mathbf{T}\left(\mathbf{J}_\mathbf{D}^\mathbf{T}-\mathbf{J}^\mathbf{T}\right)\mathbf{e}\leqslant\;&\frac{1}{4}\frac{1}{k_g}\mathbf{e}^\mathbf{T}\mathbf{P}^{-\mathbf{T}}\mathbf{P}^{-\mathbf{1}}\mathbf{e}\\
&+\frac{1}{k_g}\dot{\mathbf{q}}_\mathbf{s}^\mathbf{T}\left[\mathbf{J}_\mathbf{D}^\mathbf{T}-\mathbf{J}^\mathbf{T}\right]^\mathbf{T}\mathbf{P}^\mathbf{T}\mathbf{P}\left[\mathbf{J}_\mathbf{D}^\mathbf{T}-\mathbf{J}^\mathbf{T}\right]\dot{\mathbf{q}}_\mathbf{s}
\end{aligned}
\tag{33}
$$

where $\mathbf{P}$ is a gain matrix. Thus

$$
\begin{aligned}
\dot{V}\leqslant\;&\dot{\mathbf{x}}_\mathbf{m}^\mathbf{T}\mathbf{A}\dot{\mathbf{x}}_\mathbf{m}+\dot{\mathbf{q}}_\mathbf{s}^\mathbf{T}\mathbf{B}\dot{\mathbf{q}}_\mathbf{s}+\mathbf{e}^\mathbf{T}\mathbf{C}\mathbf{e}\\
&-\frac{\eta}{\delta}\dot{\mathbf{q}}_\mathbf{s}^\mathbf{T}\left(t-\delta\right)\mathbf{J}_\mathbf{D}^\mathbf{T}\mathbf{J_D}\dot{\mathbf{q}}_\mathbf{s}\left(t-\delta\right)+\boldsymbol{\Upsilon}_\mathbf{1}+\boldsymbol{\Upsilon}_\mathbf{2}
\end{aligned}
\tag{34}
$$

where

$$
\begin{aligned}
\mathbf{A}=\;&-\frac{1}{2}\frac{\alpha_m}{k_m}\mathbf{I}+\frac{1}{16}\bar{h}_2\mathbf{I}+\frac{1}{4}\frac{1}{\alpha_m}\mathbf{M}_\mathbf{m}^\mathbf{T}\mathbf{M_m}\\
&+\frac{1}{2}\frac{k_g}{\alpha_m}\beta\nabla_\mathbf{fp}\mathbf{M_m}+\bar{h}_1\mathbf{I}
\end{aligned}
\tag{35}
$$

$$
\begin{aligned}
\mathbf{B}=\;&-\frac{\alpha_s}{k_gk_p}\mathbf{J}_\mathbf{D}^\mathbf{T}\mathbf{J_D}+2\bar{h}_2\mathbf{J}^\mathbf{T}\mathbf{J}+\frac{1}{4}\frac{1}{\alpha_m}\mathbf{J}^\mathbf{T}\mathbf{J}\\
&+\frac{1}{4}\bar{h}_1\beta^2\mathbf{J}_\mathbf{D}^\mathbf{T}\bar{\nabla}_\mathbf{fp}\bar{\nabla}_\mathbf{fp}^\mathbf{T}\mathbf{J_D}+\frac{\eta}{\delta}\mathbf{J}_\mathbf{D}^\mathbf{T}\mathbf{J_D}\\
&+\frac{1}{2}\frac{1}{k_gk_p}(\dot{\mathbf{J}}_\mathbf{D}^\mathbf{T}\mathbf{J_D}+\mathbf{J}_\mathbf{D}^\mathbf{T}\dot{\mathbf{J}}_\mathbf{D})\mathbf{M_s}\\
&+\frac{1}{k_g}\left[\mathbf{J}_\mathbf{D}^\mathbf{T}-\mathbf{J}^\mathbf{T}\right]^\mathbf{T}\mathbf{P}^\mathbf{T}\mathbf{P}\left[\mathbf{J}_\mathbf{D}^\mathbf{T}-\mathbf{J}^\mathbf{T}\right]
\end{aligned}
\tag{36}
$$

and

$$
\mathbf{C}=-\frac{1}{2}\frac{k_m}{\alpha_m}\mathbf{I}+\frac{1}{16}\frac{k_m^2\bar{h}_2}{\alpha_m^2}\mathbf{I}+\frac{1}{4}\frac{1}{k_g}\mathbf{P}^{-\mathbf{T}}\mathbf{P}^{-\mathbf{1}}
\tag{37}
$$

are the internal terms of the quadratic variables

$$
\boldsymbol{\Upsilon}_\mathbf{1}=\frac{1}{2}\frac{\chi}{\alpha_m}\|\mathbf{e}\|\,\dot{\mathbf{x}}_\mathbf{m}^\mathbf{T}\dot{\mathbf{x}}_\mathbf{m}+\|\mathbf{e}\|\|\beta\nabla_\mathbf{fp}-\mathbf{I}\|\|\dot{\mathbf{x}}_\mathbf{m}\|
\tag{38}
$$

is a nonlinear disturbance while

$$
\boldsymbol{\Upsilon}_\mathbf{2}=\xi\|\boldsymbol{\gamma}\|\,\boldsymbol{\Theta}+\varepsilon k_a\boldsymbol{\Theta}+\frac{1}{2}\frac{1}{\alpha_m}\|\mathbf{e}\|\,\|\mathbf{f_h}\|
\tag{39}
$$

with

$$
\boldsymbol{\Theta}=\frac{1}{k_g}\|\mathbf{e}\|+\frac{1}{2}\frac{\lambda_{m_{max}}}{\alpha_m}\|\dot{\mathbf{x}}_\mathbf{m}\|+\frac{\bar{h}_1}{k_g}\|\dot{\mathbf{q}}_\mathbf{s}\|\,\|\mathbf{J_D}\|
\tag{40}
$$

represents a set of linear disturbances.

C. ANALYSIS OF $\dot{V}$

Let us analyze the first four terms of (34). These expressions include quadratic terms of the local robot velocity $\dot{\mathbf{x}}_\mathbf{m}$, remote robot velocity $\dot{\mathbf{q}}_\mathbf{s}$, coordination error between E.E. $\mathbf{e}$, and delayed velocity of the remote robot $\dot{\mathbf{q}}_\mathbf{s}(t-\delta)$. For the local robot velocity, a high value of α_m and a low value of k_m allow achieving the negativity of the internal terms of $\dot{\mathbf{x}}_\mathbf{m}^\mathbf{T}\dot{\mathbf{x}}_\mathbf{m}$. However, these values have an inverse relationship when achieving negative values for the coordination error $\mathbf{e}$.

For the joint velocities of the follower robot, the terms α_s, k_g, and k_p allow achieving the negativity of $\dot{\mathbf{q}}_\mathbf{s}^\mathbf{T}\dot{\mathbf{q}}_\mathbf{s}$. It is important to note that the damping values of the leader inversely affect the behavior of $\dot{\mathbf{q}}_\mathbf{s}$, as well as η, δ of the delayed velocities of the remote robot. This is reasonable, given that the reduction of leader velocities through α_m will limit the change in **ref**, causing the coordination error to be smaller, and therefore the change in the remote's robot velocities.

Thus, considering bounded values for $\mathbf{f_h}$ and $\mathbf{f_e}$, the appropriate configuration of α_m, α_s, k_m, k_p, k_g, k_a, $\nabla_\mathbf{fp}$, $\dot{\varepsilon}(t)$, and $\dot{\beta}(t)$ allows achieving $\mathbf{A}, \mathbf{B}, \mathbf{C} < 0$, but this analysis must be complemented with a numerical analysis to evaluate the effect of $\boldsymbol{\Upsilon_1}$ and $\boldsymbol{\Upsilon_2}$ on $\dot{\mathbf{x}}_\mathbf{m}$, $\dot{\mathbf{q}}_\mathbf{s}$, $\mathbf{e}$.

D. ANALYSIS OF PERTURBATIONS IN $\dot{V}$

Let us assume a calibration that satisfies $\mathbf{A}, \mathbf{B}, \mathbf{C} < 0$. As shown in the development of $\dot{V}$, both the nonlinear $\boldsymbol{\Upsilon_1}$ and linear perturbations $\boldsymbol{\Upsilon_2}$ will depend on the transitions and the type of selected mode.

Initially, we analyze the terms that do not depend on variables ε and β. The first term of the nonlinear perturbation $\boldsymbol{\Upsilon_1}$ results from Property 3 but can be reduced through the adjustment of α_m. Moreover, the first term of $\boldsymbol{\Upsilon_2}$ is related to the transitions, depending on $\dot{\varepsilon}(t)$ and $\dot{\beta}(t)$ (both upper-bounded by $\xi(t)$), k_a and k_g (internal elements of $\boldsymbol{\gamma}$), and $\boldsymbol{\Theta}$. The functions $\varepsilon(t)$ and $\beta(t)$ are designed to avoid discontinuities and must be sufficiently smooth to decrease the energy during the transition. However, the term $\xi\|\boldsymbol{\gamma}\|\boldsymbol{\Theta}$ of (39) is null if the leader's position is placed at the origin during the transition, reducing the effect of the transitions on the system's stability.

The remaining parameters of the linear and nonlinear perturbations are analyzed, taking into account each mode. A more precise depiction of the response of $\dot{V}$ along the system trajectories is visually presented. Figs. 3 and 4 illustrate, on each axis, a spectrum of coordination errors $\mathbf{e}$, velocities of the leading robot $\dot{\mathbf{x}}_\mathbf{m}$, and velocities of the follower robot $\dot{\mathbf{q}}_\mathbf{s}$. The values of $\dot{V}$ are visualized using a color scheme, where shades of blue correspond to more negative values and shades of yellow denote more positive values. Specifically, positive values of $\dot{V}$ are represented in red.

1) ANALYSIS OF BEHAVIOR IN NL-POSITION MODE

Let us consider that **ref** is in NL-position mode through $\beta = 1$ (after completing the transition, i.e., $\dot{\beta} = 0$). In this case, the second term of $\boldsymbol{\Upsilon_2}$ is null, and the second term of $\boldsymbol{\Upsilon_1}$ has the form $\|\mathbf{e}\|\|\nabla_\mathbf{fp} - \mathbf{I}\|\|\dot{\mathbf{x}}_\mathbf{m}\|$. This shows that the shape of the normalized function $\mathbf{f_p}(\mathbf{x_m})$ affects $\dot{V}$ through its gradient $\nabla_\mathbf{fp}$. If $\mathbf{f_p}$ is linear, its gradient is equal to the unit, and the second term of the nonlinear perturbation is null.

TABLE 2. Conditions to Evaluate $\dot{V}$ Depending on $\mathbf{e}$, $\dot{\mathbf{x}}_\mathbf{m}$, $\dot{\mathbf{x}}_\mathbf{s}$ for NL-Position Mode

Configuration	$\bar{h}_1$	$\bar{h}_2$	$\nabla_\mathbf{fp}$	k_g	k_s	k_m	α_m	α_s	f_h	f_e
A1	0	0	1	1	0.5	1	4	4	0.2	0.2
A1-h	$0.25\cos(t)+0.25$	0.5	1	1	0.5	1	4	4	0.2	0.2
A2-h	$0.25\cos(t)+0.25$	0.5	1	1	0.5	1	10	10	0.2	0.2
B1	0	0	1.5	10	0.5	1	10	10	0.2	0.2
B1-h	$0.25\cos(t)+0.25$	0.5	1.5	10	0.5	1	9.75	9.75	0.2	0.2
B2-h	$0.25\cos(t)+0.25$	0.5	1.5	10	0.5	1	16	16	0.2	0.2

To determine the response of the system in this mode, we propose six configurations, as shown in Table 2. These configurations illustrate the system's behavior with and without time delay for the position mode, considering different parameters of the mapping and controllers. We numerically evaluate the behavior of $\dot{V}$ depending on $\mathbf{e}$, $\dot{\mathbf{x}}_\mathbf{m}$, and $\dot{\mathbf{q}}_\mathbf{s}$ for the selected parameter combinations (A1, A1-h, A2-h, B1, B1-h, and B2-h). Subsequently, we present this through color variations in Fig. 3, where values closer to zero for $\dot{V}$ are represented by light yellow while more negative values tend toward dark blue. For configurations A1 and B1, the bounding of $\mathbf{e}$, $\dot{\mathbf{x}}_\mathbf{m}$, and $\dot{\mathbf{q}}_\mathbf{s}$ is achieved because $\dot{V}$ takes negative values away from the origin for these nondelayed cases. On the other hand, with similar parameters, the time delays in A1-h and B1-h cause zones that do not guarantee energy dissipation, highlighted with red dots. To solve this problem, the developed theoretical analysis provides guidelines to ensure stability by simultaneously adjusting the parameters of mapping and controllers, as demonstrated for A2-h and B2-h. Despite the time delay, the recalibration of parameters avoids zones with positive $\dot{V}$, ensuring bounded velocities and errors in the teleoperation system.

2) ANALYSIS OF BEHAVIOR IN RATE MODE

Now, let us consider that **ref** is in rate mode through $\varepsilon = 1$ (after completing the transition, i.e., $\dot{\varepsilon} = 0$). In rate mode, the second term of the linear perturbation $\boldsymbol{\Upsilon_2}$ is activated but can be regulated through the gain constant k_a. This is reasonable because a configuration of k_a with a high value will generate large values of **ref**, and therefore, the coordination errors will grow, not ensuring the bounding of $\mathbf{e}$. The selection criteria for k_a involve a tradeoff, given that, a higher k_a value enables faster movement of the robot but undermines stability while a lower k_a value enhances stability albeit with a reduction in the follower robot's velocities. Additionally, the second term of $\boldsymbol{\Upsilon_1}$, i.e., $\|\mathbf{e}\|\|\dot{\mathbf{x}}_\mathbf{m}\|$ remains active and must be compensated with the calibration of constants in $\mathbf{A}$, $\mathbf{B}$, and $\mathbf{C}$.

Similar to the NL-position mode, we propose six configurations depicted in Table 3 for different time delays, considering various parameters of the mapping and controller. Graphically, the behavior of $\dot{V}$ is visualized in Fig. 4, where lighter colors indicate a tendency toward zero for the time derivative

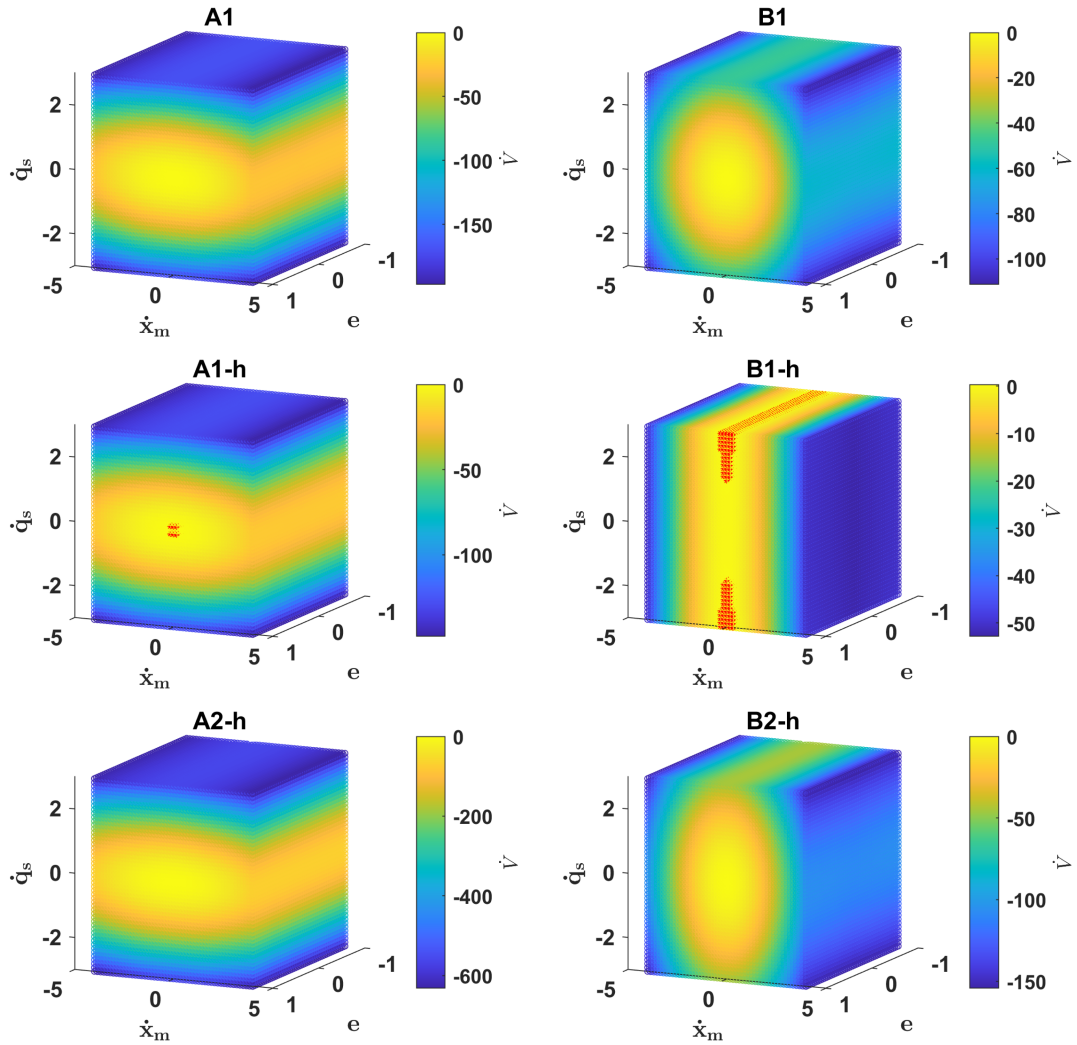

FIGURE 3. Analysis of the behavior of $\dot{V}$ along the trajectories of the system in position mode: Values tending toward dark blue are more negative. Red-colored points indicate areas where energy dissipation is not guaranteed.

TABLE 3. Conditions to Evaluate $\dot{V}$ Depending on e, $\dot{x}_m$, $\dot{x}_s$ for Rate Mode

Condition	$\bar{h}_1$	$\bar{h}_2$	k_a	k_s	k_m	α_m	α_s	f_h	f_e
A1	0	0	0.01	0.5	1	12	10	0.2	0.2
A1-h	$0.25cos(t)+0.25$	0.5	0.01	0.5	1	12	10	0.2	0.2
A2-h	$0.25cos(t)+0.25$	0.5	0.01	0.5	1	30	10	0.2	0.2
B1	0	0	1.5	0.5	1	13	5	0.2	0.2
B1-h	$0.25cos(t)+0.25$	0.5	1.5	0.5	1	13	5	0.2	0.2
B2-h	$0.25cos(t)+0.25$	0.5	1.5	0.5	1	40	40	0.2	0.2

of the Lyapunov candidate while darker colors imply more negative values of $\dot{V}$. For case B1, the provided value for k_a yields zones where energy dissipation is not guaranteed (highlighted in red), areas that grow when time delays are induced, as seen in cases A1-h, B1-h, and B2-h. However, by simultaneously calibrating the controller and mapping parameters based on the developed theoretical analysis, it is possible to achieve $\dot{V}$ values lower than or equal to zero for both nondelayed cases, such as A2-h, and delayed situations, such as B2-h, thus ensuring bounded errors and velocities.

IV. EXPERIMENTAL EVALUATION

A. EXPERIMENT SETUP AND TASK DESCRIPTION

Robots: At the local site, the haptic device used to generate control commands is the Novint Falcon, which also provides force feedback in three Cartesian axes. The leader's workspace is normalized to 9 cm per axis, and it also features buttons used to start the experiments and switch between rate and NL-position modes. At the remote site, the robotic system is a simulated Dual Mobile Manipulator with Torso (DMMT) in Gazebo-ROS2 (as shown in Fig. 5), where its right manipulator is used for experiments, defining the follower robot as a mobile manipulator with torso (MMT). The mobile platform of the MMT is of the skid-steering type [13] while the torso consists of two degrees of freedom, the first rotating about the Z-axis and the second about the Y-axis. The manipulator has 6 degrees of freedom. The designed controller considers the E.E. of the right arm as the point of interest. The workspace of the torso-manipulator set with the static mobile part is approximately 60 cm while with the movement of the platform,

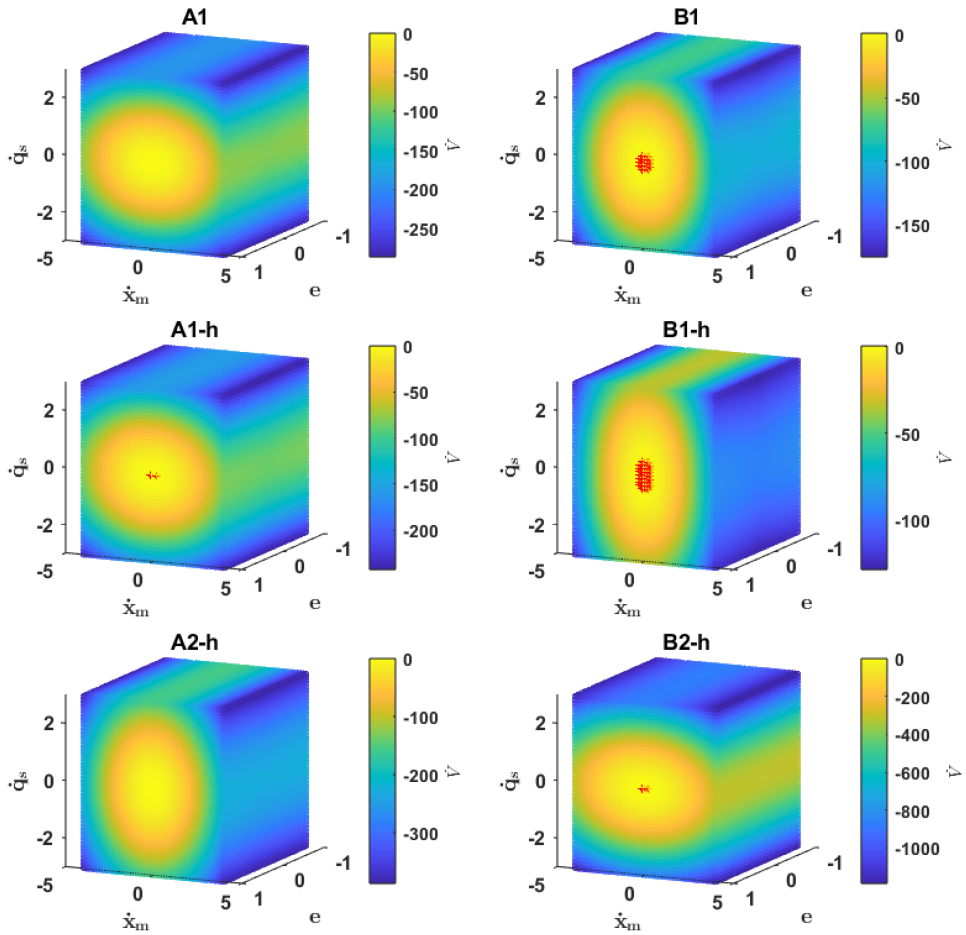

FIGURE 4. **Analysis of the behavior of $\dot{V}$ along the trajectories of the system in rate mode: Values tending toward light yellow are more positive while red-colored points indicate areas where energy dissipation is not guaranteed.**

the workspace is limited only in the Z-axis in a range from the floor until 1.20 m.

Operators: Five operators with experience in bilateral teleoperation are considered to perform the tasks. One of the operators is female, and all have an average age of 33 years, with all being right-handed.

Task Description: As a case study, the task to be executed is based on capturing, transporting, and placing an object. The task can be divided into two subtasks: 1) task-A: move the E.E. of the follower robot from a starting point to target A (position where the object is captured for transportation) and 2) task-B: move the E.E. of the MMT from target A to target B (place where the transported object is released). Considering that the robot always starts from the same initial position, the operator is suggested to move the entire robotic mechanism toward the target object. This movement is achieved through the rate mode. Once near the first target, the follower's E.E. must be positioned close to the point A with low velocity, allowing for the automatic grip of a near object. This part of the test can be executed either in rate mode or position mode, to get more accuracy in the motion. Subsequently, the second target is marked in the scenario, assuming the point where the captured object should be released. This part of the test assumes a similar execution to task-A. It is established that the targets are considered reached when the follower's E.E. is within a radius of approximately 0.02 [m] from the center of the indicated target, with a velocity lower than 0.01 [m/s]. A button on the haptic device allows the operator to start the test, activating a timer to subsequently determine the time required for the complete task execution. The timer stops when reaching target B. The selection between rate and NL-position modes is free for each operator and is not limited in any way.

Instructions: Prior to being briefed on the task to be executed, operators are free to navigate the scenario and execute commands to control the follower robot's E.E. either in rate or position mode for approximately 15 min. During this time, free tests with and without time delays are also conducted. This familiarization encompasses both strategies: the one proposed in this work and one selected from the literature. Considering that the haptic device is in a comfortable location and both haptic and visual feedback are appropriate, operators are informed of the task, clarifying that they have the freedom to choose the mapping mode, and that the objective of the task

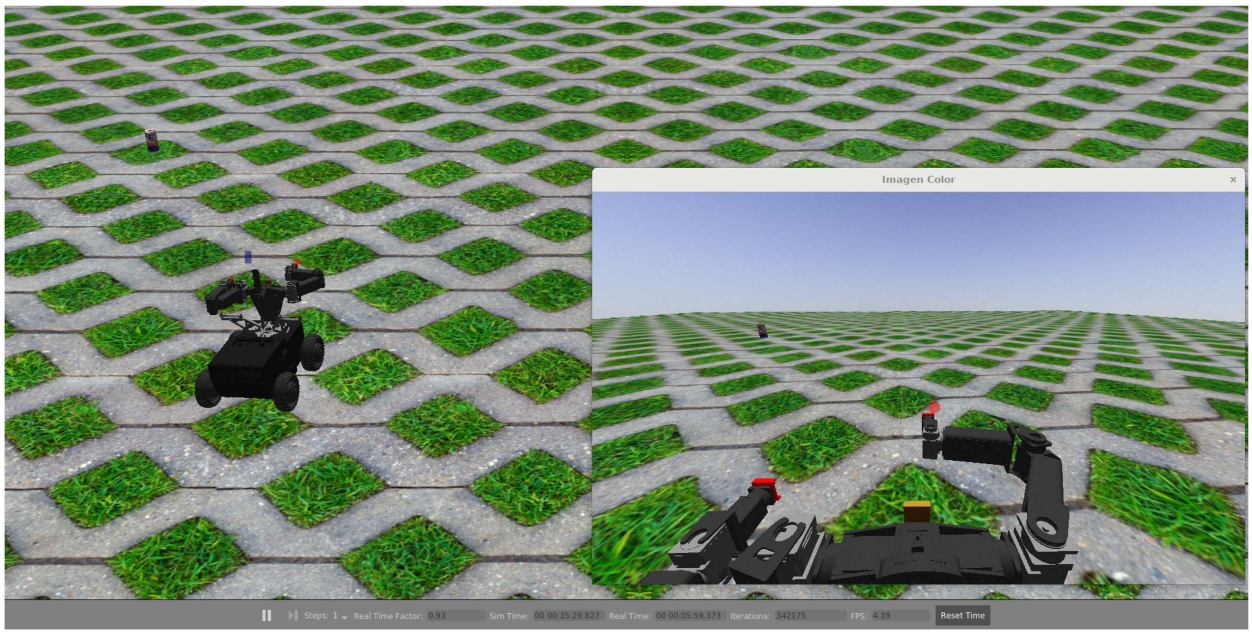

FIGURE 5. Simulation of a DMMT-type robot in the Gazebo-ROS2 environment. On the right, an image displaying information from a camera located on the robot's torso; on the left, a third-person image of the robot interacting with the environment.

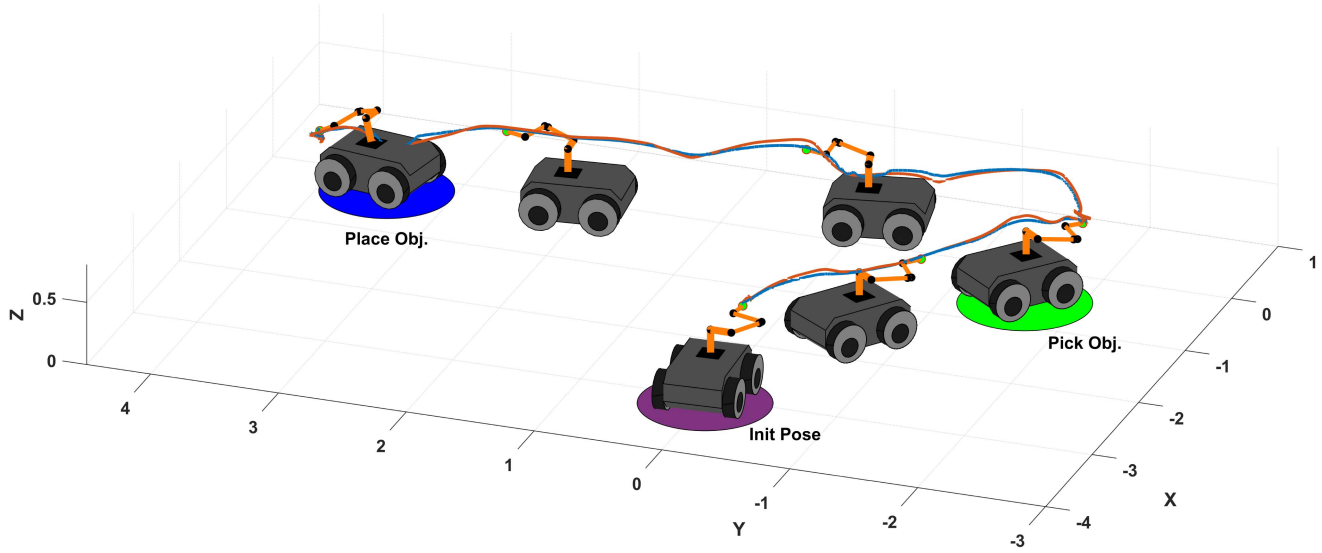

FIGURE 6. Execution reconstruction while performing a pick-and-place task. The test establishes consistent positions for all executions, with the robot's initial position set at [−3.0, 0.0, 0.5], the object's capture location at [0.0, −2.0, 0.6], and the object release position at [−0.2, 4.0, 0.35].

is to reach and release the object at the designated positions in the shortest possible time. Subsequently, each operator is instructed to perform the task, where either strategy, with or without time delay, may be randomly presented. This is done to prevent execution by memorization. For each operator, a minimum of 10 complete executions is required for each strategy and with each time delay, results that are subsequently statistically evaluated. Executions exceeding 250 s are not considered.

B. TASK RECONSTRUCTION

Reconstructing two of the executed tasks provides insight into the overarching behavior of the proposed bilateral teleoperation system. Fig. 6 illustrates the stroboscopic movement of the robot, indicating its initial position, progression toward capturing the object, and subsequent placement at the designated point. The norm of the coordination errors is shown in Fig. 7 while the norm of velocities for both the local and remote robots is depicted in 8 and 9, respectively. Changes

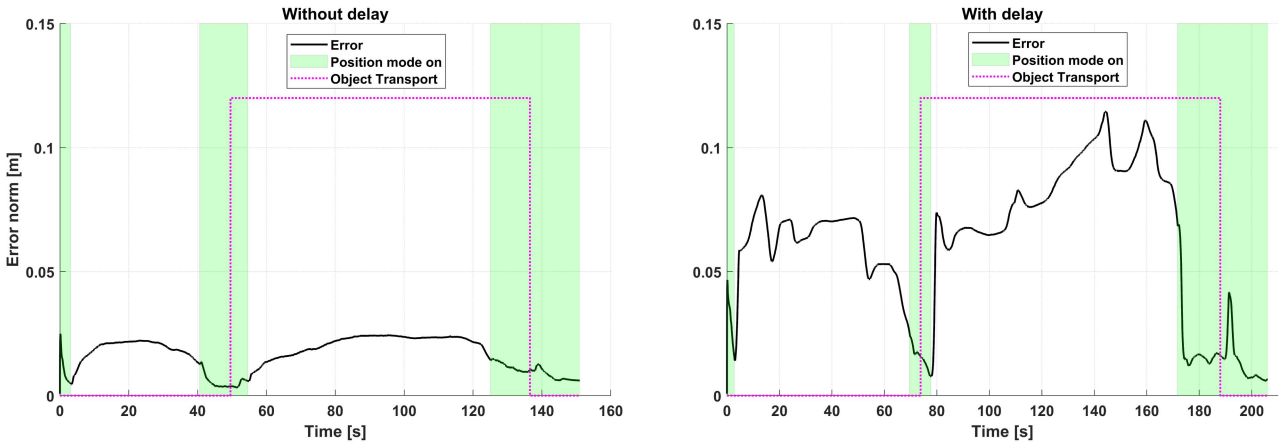

FIGURE 7. Euclidean norm of the tracking error for a pair of executed tasks, with and without time delay.

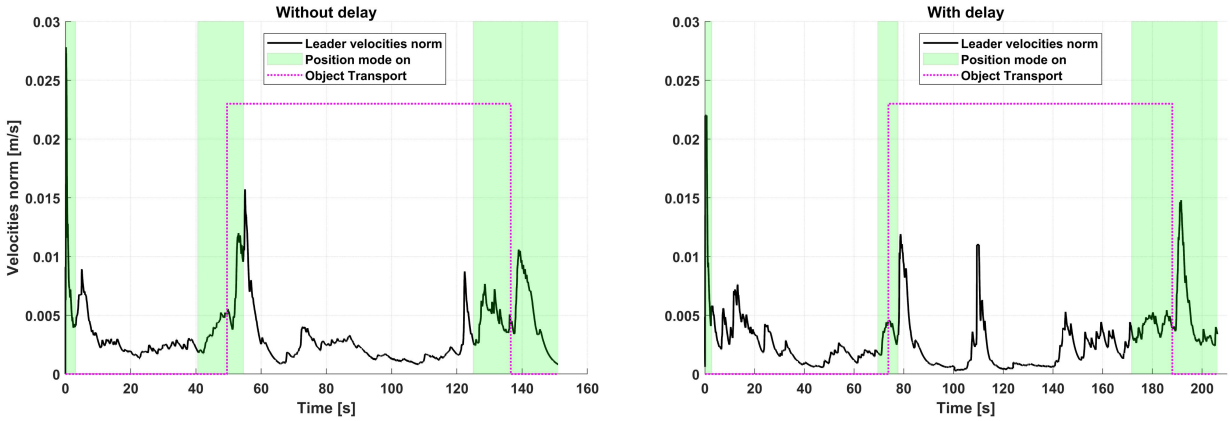

FIGURE 8. Euclidean norm of leader robot E.E. velocities, indicating when each mode is activated.

to nonlinear-position mode are indicated with green shading. The norm of the coordination errors between the E.E. for both robots shows that, although errors are bounded in both cases, an increase is noticeable when a time delay is considered (as will be further demonstrated through statistical analysis). In Fig. 8, a decrease in the norm of the E.E. Cartesian velocity of the local robot is observed when the execution includes delays, due to additional damping being injected in this case. Fig. 9 illustrates the behavior of the velocities of the remote robot. Since we consider an articular controller for the MMT, the follower robot's velocities are depicted in three parts: the dashed red and blue lines indicate the linear and angular velocities of the mobile platform, respectively, while the black line represents the norm of the robotic manipulator-torso set's articular velocities. Given the task protocol, it is noteworthy to mention that in position mode (utilized for reaching and releasing the object), the follower's velocities tend to zero upon reaching each target. For instance, in the execution without delay: Approximately at $t = 51$ s (for capturing) and $t = 135$ s (for releasing); while for the execution with delay: approximately at $t = 73$ s (for capturing) and $t = 192$ s (for releasing). Finally, Fig. 10 illustrates the norm of the force feedback experienced by the human operator. The right part displays the effect induced by time delays, with maximum values reaching up to 9 N, whereas the haptic response to tasks without time delay typically does not exceed 5 N.

With the aim of demonstrating the operation of the entire bilateral teleoperation system, a video has been included at https://youtu.be/PjtSxeigUeM. This video showcases both robots, the force feedback experienced by the human operator, and the coordination errors between the E.E. of the local robot and the remote robot, both with and without time delays.

C. PERFORMANCE ANALYSIS: COMPARISON TO AN ALTERNATIVE STRATEGY

1) ADAPTATION OF PEPE ET AL.'S APPROACH TO OUR ROBOTS

Diverse strategies for continuously transitioning between rate and position mappings have been proposed in the literature (as shown in Table 1). Specifically for mobile manipulators, Pepe et al. [21] proposed splitting the workspace of the leader robot into three radii: an outer radius R_m containing an intermediate

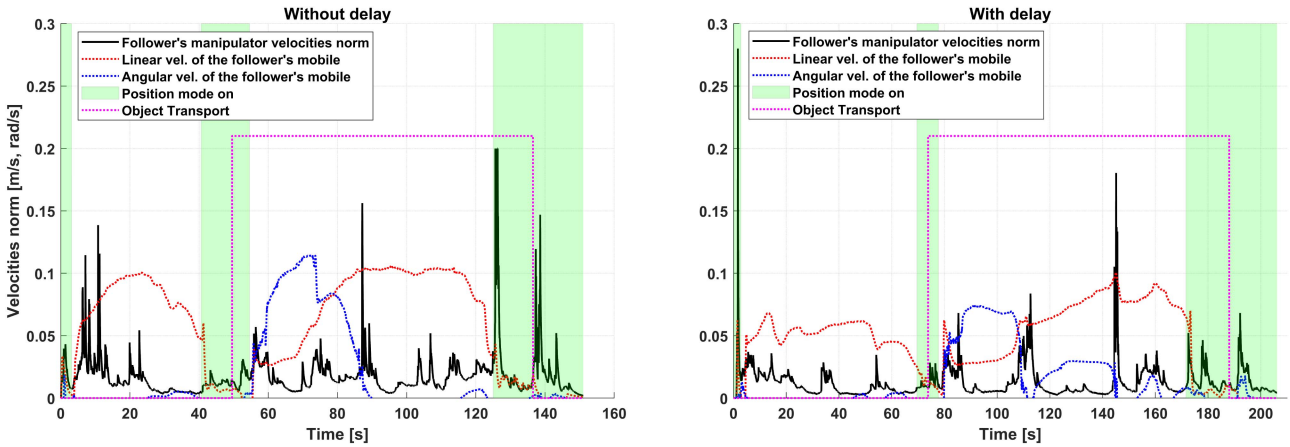

FIGURE 9. Euclidean norm of follower robot velocities. The dashed red and blue lines correspond to the linear and angular velocity of the mobile platform, respectively. The solid black line corresponds to the norm of the joint velocities of the torso-manipulator set.

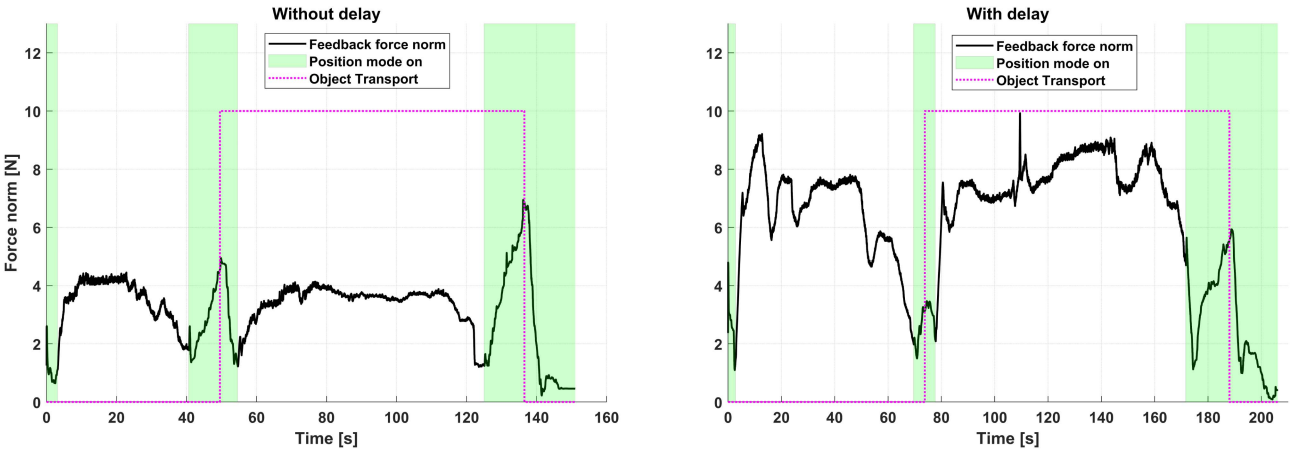

FIGURE 10. Euclidean norm of the feedback force.

TABLE 4. Configuration Parameters to Replicate the Experimentation of Pepe et al. [21]

Variable	Value	Unit	Variable	Value	Unit
R_m	0.045	[m]	δ	5.26	
R_s	0.2	[m]	R_i	0.035	[m]
R_o	0.038	[m]	$V_{\max}$	0.15	[m/s, rad/s]

TABLE 5. Parameters Used in Our Proposal

Variable	Value	Unit	Description
α_m	100	[N.s/m]	Damping applied to the leader robot
α_s	3.5	[N.s/m]	Damping applied to the follower robot
k_m	25	[N/m]	Damping applied to the leader robot
k_p	1	[N/m]	Damping applied to the follower robot
k_a	0.5		Mapping constant
k_b	1		Mapping constant
k_g	2		Mapping constant
h_1	0, 0.5	[s]	Forward delay
h_2	0, 0.5	[s]	Backward delay
V_{max}	0.15	[m/s, rad/s]	Max. velocity applied to the mobile platform
T_s	0.01	[s]	Sampling time
N_{max}	8.9	[N]	Max. force output of the haptic device

one R_o, which in turn contains an inner radius R_i. In this way, it is proposed to control the follower's E.E. when the leader's E.E. is positioned within an inner radius R_i while controlling the movement of the mobile platform in the area bounded by the radii R_o and R_m. The region between R_i and R_o is used for smooth transitioning between rate and scaled-position modes. The strategy given in [21] (Pepe strategy) has been implemented in this work to compare its performance with our proposal (our strategy), where the parameters shown in Table 4 have been calibrated to apply [21] to our robots: the Falcon Novint haptic device (leader robot) and a follower composed by a custom mobile and the Manipulator-H provided by Robot is: https://emanual.robotis.com/docs/en/platform/openmanipulator_p/ros_simulation/. The parameters used in our proposal are shown in Table 5.

TABLE 6. Table Comparing Objective Metrics From the Experimental Data

Metrics	Unit	S.M.	Without delay		With delay	
			Pepe *et al.* [21]	Proposed	Pepe *et al.* [21]	Proposed
T_{task}	[s]	Mean SD CI	151.50 13.79 [145.22, 157.78]	127.45 7.39 [123.78, 131.13]	211.51 23.74 [200.40, 222.62]	164.94 14.74 [157.61, 172.27]
End-effector Coord. Error	[mm]	Mean SD CI	20.52 1.22 [19.98, 21.06]	15.90 0.81 [15.50, 16.31]	83.13 19.93 [72.05, 94.21]	72.69 5.57 [69.91, 75.46]
Vels. Coord. Error *	[mm/s, mrad/s]	Mean SD CI	3.57, 11.07 0.51, 1.12 [3.34, 3.80], [10.56, 11.58]	- - - -	10.28, 18.68 2.08, 3.12 [9.30, 11.25], [17.22, 20.14]	- - - -
Feedback force	[N]	Mean SD CI	5.83 0.51 [5.59, 6.06]	3.61 0.12 [3.56, 3.67]	4.47 0.57 [4.20, 4.73]	5.35 0.27 [5.22, 5.48]
Leader vels.	[mm/s]	Mean SD CI	6.08 0.93 [5.65, 6.50]	4.86 0.33 [4.70, 5.03]	5.56 0.91 [5.13, 5.98]	4.50 1.09 [3.96, 5.04]
Follower vels.: Mobile *	[mm/s, mrad/s]	Mean SD CI	55.37, 10.12 5.25, 1.10 [52.98, 57.76], [9.62, 10.62]	69.53, 12.75 4.01, 0.94 [67.54, 71.52], [12.28, 13.22]	40.23, 7.34 4.40, 0.80 [38.17, 42.29], [6.97, 7.72]	53.08, 10.59 4.69, 1.14 [50.75, 55.42], [10.09, 11.16]
Follower vels.: Manipulator	[mrad/s]	Mean SD CI	50.96 7.12 [47.72, 54.20]	44.69 5.05 [42.18, 47.20]	53.04 11.07 [47.86, 58.22]	43.33 7.41 [38.64, 46.02]

*Presented as: linear velocity, angular velocity.

Results encompass all five operators, both strategies, and tests with and without time delays.

For a fair comparison, the protocol for executing a pick-and-place task of an object remains consistent. A set of executions involving human operators is conducted for both cases: with and without time delay. Subsequently, valid executions are analyzed considering the following objective metrics: time to complete the task (T_{task}), coordination error between the robots' E.E., force feedback, and velocities of both robots. Table 6 presents the statistical measurements of this comparison, calculating the mean, standard deviation (SD), and confidence interval at 95% (CI).

2) DESCRIPTION OF THE METRICS CONSIDERED

The time required to complete a task is influenced by each operator's ability to translate and position the follower robot's E.E. over the indicated targets. On the other hand, the task coordination error is calculated through the difference between the reference generated by the local robot's mapping and the position of the follower robot's E.E.. For our proposal, the defined controller requires knowledge of $\mathbf{x_s}$; therefore, we have a continuous measurement of the position of the remote robot's E.E. However, for Pepe et al. [21], the E.E. of the manipulator robot (mounted on the mobile platform) is exclusively utilized in the position mode. Within this mode, position errors are computed between the reference generated by the local robot and the position of the follower's E.E. (depicted in the same row as the coordination errors of our proposal). Regarding the rate mode, we compute velocity coordination errors and include them in an additional row to illustrate their performance in the experiments. Moreover, for our case, force feedback depends on damping and coordination errors between E.E. while haptic feedback for Pepe et al. [21] is only activated in the rate mode, where higher velocity injected into the mobile platform results in greater force perceived by the human operator. Finally, E.E. velocities in Cartesian space are measured in the local robot, whereas for the remote robot, linear and angular velocities for the mobile platform and joint velocities for the manipulator are distinguished.

D. COMPARISON BETWEEN STRATEGIES

The main advantage of our strategy compared to that of Pepe et al. [21] is reflected in the significant reduction of the Time to complete the task (about 20%). The proposed scheme entails the application of force feedback and control actions on the follower robot, contingent upon the calibration of parameters within the local controller, remote controller, and mapping function. This framework is substantiated by the theoretical findings presented in Section III. In agreement with this result, Table 6 shows a reduction in the kinetic energy of the leader due to an increase in force feedback for executions with delay. This leads to a reduction in the velocity of the mobile manipulator, effectively bounding the coordination errors within the bilateral teleoperation system.

Furthermore, it is worth noting that in Pepe et al.'s strategy, the calibration of force feedback and mapping occurs independently of a theoretical stability analysis. In this approach, the transition between control modes (rate/position) is gradual

and contingent upon the leader's position. Despite its simplicity in implementation, we have encountered challenges when teleoperating the remote robot using the Pepe strategy. Specifically, when attempting to maneuver the mobile platform, the designed mapping necessitates extending the arm initially, resulting in heightened coordination errors and prolonged task completion times.

In summary, as depicted in Table 6, our strategy enhances system performance measured in terms of coordination error and task completion time, both with and without time delay.

V. CONCLUSION

This article presents a stability analysis of a bilateral teleoperation system for a mobile manipulator, considering time delays and incorporating rate/nonlinear-position mapping. Utilizing Cartesian/articular controllers structured on P+d frameworks, we have formulated a continuous function that maps the position of the leader robot, operating within a confined workspace, into reference commands for the follower robot situated in a more extensive workspace. As the main contribution, a theoretical analysis grounded in Lyapunov–Krasovskii principles, substantiated through numerical evaluations and human-in-the-loop experiments under time delays, has been conducted to discern the impact of mapping and controller parameters on constraining the velocities of the leader and follower robots, as well as the coordination error between them. The Lyapunov–Krasovskii functional proposed allows obtaining a partial result where linear and nonlinear perturbations appear against quadratic terms, with matrices **A** (35), **B** (36), and **C** (37) that can be negative definite by calibrating α_m, α_s, and the relation $\frac{k_m}{\alpha_m}$, depending on the time-varying delay. The numerical analysis is performed by evaluating the time derivative of the proposed functional considering the nonlinear and linear perturbations. Primarily, the rate and transitions parameters of the mapping and human operator force modify such perturbations. This article collaborates to confirm, with scientific support, that as the human force ($\mathbf{f_h}$) is greater, the transition is more abrupt, and the rate gain (k_a) is higher, the coordination error ($\mathbf{e}$) is bigger. Furthermore, the series of experiments conducted reveals that force feedback constrains the mobility of the leading robot. This limitation stems from the escalating coordination error between the rate/NL-position mapping and the positional accuracy of the follower robot's E.E., attributed to time delays or the remote robot's interaction with its surroundings. Hence, we highlight the utility of integrating rate/nonlinear-position mapping alongside Cartesian/articular controllers in the delayed bilateral teleoperation of mobile manipulators, where the inclusion of an additional degree of freedom (independent of the leader's E.E. position or environmental characteristics) is used to achieve mode transition in our work. The proposed scheme facilitates the operation of redundant systems utilizing haptic devices with restricted degrees of freedom.

Part of our future work will include analyzing the performance of the proposal with various switching methods, aiming to demonstrate the generalization of our strategy to diverse applications. Moreover, experiments involving pick-and-place tasks with various types of objects and unstructured environments, using a real mobile manipulator, will be conducted to evaluate practical performance. Furthermore, the proposed bilateral teleoperation scheme is designed to be extended to the teleoperation of a real mobile dual manipulator. Accordingly, further research will involve extending the rate/NL-position mapping to control a primary manipulator and developing another mapping to control a secondary E.E. This extension will be evaluated for its behavior through stability analysis and experimentation.

APPENDIX A MODIFIED JACOBIAN

Given a full-rank Jacobian matrix $\mathbf{J}$, its pseudoinverse is computed using the Moore–Penrose method with the inclusion of a weight matrix $\mathbf{W}$, resulting in: $\mathbf{J}^{\dagger} = \mathbf{W^{-1}J^{T}}(\mathbf{JW^{-1}J^{T}})^{-1}$. The Jacobian can be treated through singular value decomposition (SVD) as

$$\mathbf{J} = \mathbf{UPV^{T}} = \sum_{i=1}^{r} \rho_i \mathbf{u}_i \mathbf{v}_i^T \tag{41}$$

having $r = \max_i\{i|\rho_i > 0\}$, all eigenvalues greater than zero are located on the main diagonal of $\mathbf{P}$, $\mathbf{U}$, and $\mathbf{V}$ are orthonormal matrices while $\mathbf{u}_i$ and $\mathbf{v}$ are the columns of $\mathbf{U}$ and $\mathbf{V}$, respectively. This decomposition can be used to modify the eigenvalues ρ_i, using quadratic damping, singular value filtering, and error damping, among others [31]. The selection of these methods is beyond our scope. Therefore, we use $\mathbf{J_D}$ as the Damped Jacobian in the form [31]

$$\mathbf{J_D} = h_{\nu,\rho_0}(\rho_i)\mathbf{u}_i\mathbf{v}_i^T \tag{42}$$

where

$$h_{\nu,\rho_0}(\rho) = \frac{\rho^3 + \nu\rho^2 + 2\rho + 2\rho_0}{\rho^2 + \nu\rho + 2} \tag{43}$$

and ν is a configurable shape factor and ρ_0 is the minimum value imposed as the lowest eigenvalue.

APPENDIX B POSITIVITY OF THE CANDIDATES

A. POSITIVITY OF V_1

Considering

$$\mathbf{a^{T}b} \leqslant \mathbf{a^{T}a} + \mathbf{b^{T}b} \tag{44}$$

the condition for part of V_1 to be positive definite is

$$2k_4\mathbf{e^{T}M_m\dot{x}_m} \leqslant \frac{1}{2}k_1\mathbf{e^{T}e} + \frac{1}{2}k_2\mathbf{\dot{x}_m^{T}M_m\dot{x}_m}. \tag{45}$$

Taking into account Property 1, the worst case scenario to meet is $2k_4\lambda_{m_{\max}}\mathbf{e^{T}\dot{x}_m} \leqslant \frac{1}{2}k_1\mathbf{e^{T}e} + \frac{1}{2}k_2\lambda_{m_{\min}}\mathbf{\dot{x}_m^{T}\dot{x}_m}$. According to (44), let us define the components $\mathbf{a} = \sqrt{k_1}\mathbf{e}$ and $\mathbf{b} = \sqrt{k_2}\sqrt{\lambda_{m_{\min}}}\mathbf{\dot{x}_m}$, which allows us to determine the conditions for k_1, k_2, and k_4. Noticing that the inequality (45) holds if

$$2k_4\lambda_{m_{\max}}\mathbf{e^{T}\dot{x}_m} \leqslant \sqrt{k_1}\sqrt{k_2}\sqrt{\lambda_{m_{\min}}}\mathbf{e^{T}\dot{x}_m} = \mathbf{a^{T}b}$$

where $k_4 \leqslant \frac{1}{2}\sqrt{k_1}\sqrt{k_2}\sqrt{\frac{\lambda_{m_{\min}}}{\lambda^2_{m_{\max}}}}$. Now, considering the given values for the constants k_1, k_2, and k_4 in the development of $\dot{V}_1$, we have

$$\frac{1}{4}\frac{1}{\alpha_m} \leqslant \frac{1}{2}\sqrt{\frac{1}{4}\frac{1}{k_m}}\sqrt{\frac{1}{k_g}}\sqrt{\frac{\lambda_{m_{\min}}}{\lambda^2_{m_{\max}}}}.$$

Simplifying, the final inequality is established as

$$\alpha_m \geqslant \sqrt{k_m}\sqrt{k_g}\sqrt{\frac{\lambda^2_{m_{\max}}}{\lambda_{m_{\min}}}}. \tag{46}$$

Note that α_m adjusts the damping, which bounds the velocities of the follower robot, so (46) ensures that (45) is satisfied, since the higher α_m is, the lower k_4 will be.

B. POSITIVITY OF V_2

For V_2, consider the term $\frac{1}{2}k_3\dot{\mathbf{q}}_s^{\mathbf{T}}\mathbf{J}_{\mathbf{D}}^{\mathbf{T}}\mathbf{J}_{\mathbf{D}}\mathbf{M}_{\mathbf{s}}\dot{\mathbf{q}}_s$. Considering $\mathbf{J}_{\mathbf{D}}^{\mathbf{T}}\mathbf{J}_{\mathbf{D}}$ and $\mathbf{M}_{\mathbf{s}}$ as positive definite, their multiplication does not guarantee positive definiteness, i.e., in the most unfavorable scenario, the inner product of

$$\dot{\mathbf{q}}_s^{\mathbf{T}}\mathbf{J}_{\mathbf{D}}^{\mathbf{T}}\mathbf{J}_{\mathbf{D}}\mathbf{M}_{\mathbf{s}}\dot{\mathbf{q}}_s$$

could be less than zero.

The proposed V_2 in (13) includes the fourth term, where δ and η can be configured to ensure that

$$\frac{1}{2}k_4\dot{\mathbf{q}}_s^{\mathbf{T}}\mathbf{J}_{\mathbf{D}}^{\mathbf{T}}\mathbf{J}_{\mathbf{D}}\mathbf{M}_{\mathbf{s}}\dot{\mathbf{q}}_s + \frac{\eta}{\delta}\int_{t-\delta}^{t}\dot{\mathbf{q}}_s^{\mathbf{T}}\mathbf{J}_{\mathbf{D}}^{\mathbf{T}}\mathbf{J}_{\mathbf{D}}\dot{\mathbf{q}}_s \geqslant 0. \tag{47}$$

Therefore, considering $k_3 = \frac{1}{k_g k_p}$ from the development of $\dot{V}$, $\delta > 0$, and Property 1, we can configure $\eta > \frac{1}{2}\frac{1}{k_g k_p}\lambda_{m_{\max}}$ in order to satisfy (47).

REFERENCES

[1] K. Darvish et al., "Teleoperation of humanoid robots: A survey," *IEEE Trans. Robot.*, vol. 39, no. 3, pp. 1706–1727, Jun. 2023.

[2] F. A. Chicaiza, E. Slawiñski, L. R. Salinas, and V. A. Mut, "Evaluation of path planning with force feedback for bilateral teleoperation of unmanned rotorcraft systems," *J. Intell. Robot. Syst.*, vol. 105, no. 2, 2022, Art. no. 34.

[3] M. del Carmen Claudio, V. Moya, E. Slawinski, and V. Mut, "Simultaneous motion and shape control of redundant mobile manipulators," *Int. J. Eng. Insights*, vol. 1, no. 1, pp. 19–24, 2023.

[4] L. Antonyshyn, J. Silveira, S. Givigi, and J. Marshall, "Multiple mobile robot task and motion planning: A survey," *ACM Comput. Surv.*, vol. 55, no. 10, pp. 1–35, 2023.

[5] S. Thakar et al., "A survey of wheeled mobile manipulation: A decision-making perspective," *J. Mechanisms Robot.*, vol. 15, no. 2, 2023, Art. no. 020801.

[6] T. Hernandez, E. Nuno, and A. Y. Alanis, "Teleoperation of mobile manipulators with non-holonomic restrictions," in *Proc. IEEE 13th Int. Conf. Netw., Sens., Control*, 2016, pp. 1–6.

[7] D. Sun, A. Kiselev, Q. Liao, T. Stoyanov, and A. Loutfi, "A new mixed-reality-based teleoperation system for telepresence and maneuverability enhancement," *IEEE Trans. Human-Mach. Syst.*, vol. 50, no. 1, pp. 55–67, Feb. 2020.

[8] C. N. Mokogwu and K. Hashtrudi-Zaad, "A hybrid position–rate teleoperation system," *Robot. Auton. Syst.*, vol. 141, 2021, Art. no. 103781.

[9] M. J. Voskuil, "Hybrid design combining position and rate control allows intuitive workspace extension for teleoperation," Ph.D. dissertation, Delft Univ. Technol., Delft, The Netherlands, 2015.

[10] I. Farkhatdinov and J.-H. Ryu, "Hybrid position-position and position-speed command strategy for the bilateral teleoperation of a mobile robot," in *Proc. Int. Conf. Control, Automat., Syst.*, 2007, pp. 2442–2447.

[11] L. Liu, G. Liu, Y. Zhang, and D. Wang, "A modified motion mapping method for haptic device based space teleoperation," in *Proc. IEEE 23rd Int. Symp. Robot Hum. Interactive Commun.*, 2014, pp. 449–453.

[12] W. Bu, G. Liu, and C. Liu, "Rate-position-point hybrid control mode for teleoperation with force feedback," in *Proc. Int. Conf. Adv. Robot. Mechatron.*, 2016, pp. 420–425.

[13] J. Moreno, E. Slawiñski, F. A. Chicaiza, F. G. Rossomando, V. Mut, and M. A. Morán, "Design and analysis of an input–output linearization-based trajectory tracking controller for skid-steering mobile robots," *Machines*, vol. 11, no. 11, 2023, Art. no. 988.

[14] Z. Chen, F. Huang, W. Sun, and W. Song, "An improved wave-variable based four-channel control design in bilateral teleoperation system for time-delay compensation," *IEEE Access*, vol. 6, pp. 12848–12857, 2018.

[15] H. Su, W. Qi, C. Yang, J. Sandoval, G. Ferrigno, and E. D. Momi, "Deep neural network approach in robot tool dynamics identification for bilateral teleoperation," *IEEE Robot. Autom. Lett.*, vol. 5, no. 2, pp. 2943–2949, Apr. 2020.

[16] E. Nuño, L. Basañez, and R. Ortega, "Passivity-based control for bilateral teleoperation: A tutorial," *Automatica*, vol. 47, no. 3, pp. 485–495, 2011.

[17] D. D. Santiago, E. Slawiñski, L. R. Salinas, and V. A. Mut, "Force and position coordination for delayed bilateral teleoperation of a manipulator robot," *Int. J. Dyn. Control*, vol. 12, pp. 1679–1693 , 2023.

[18] J. Barrio, M. Ferre, F. Suárez-Ruiz, and R. Aracil, "A remote handling rate-position controller for telemanipulating in a large workspace," *Fusion Eng. Des.*, vol. 89, no. 1, pp. 25–28, 2014.

[19] J. Han and G.-H. Yang, "Improving teleoperator efficiency using position–rate hybrid controllers and task decomposition," *Appl. Sci.*, vol. 12, no. 19, 2022, Art. no. 9672.

[20] A. Khalifa, A. Ramadan, K. Ibrahim, M. Fanni, S. Assal, and A. Abo-Ismail, "Workspace mapping and control of a teleoperated endoscopic surgical robot," in *Proc. 19th Int. Conf. Methods Models Automat. Robot.*, 2014, pp. 675–680.

[21] A. Pepe, D. Chiaravalli, and C. Melchiorri, "A hybrid teleoperation control scheme for a single-arm mobile manipulator with omnidirectional wheels," in *Proc. IEEE/RSJ Int. Conf. Intell. Robots Syst.*, 2016, pp. 1450–1455.

[22] L. Guanyang, G. Xuda, L. Lingzhi, and W. Yan, "Haptic based teleoperation with master-slave motion mapping and haptic rendering for space exploration," *Chin. J. Aeronaut.*, vol. 32, no. 3, pp. 723–736 , 2019.

[23] S. Gou, J. Zhou, H. Zhang, M. Liu, S. Yang, and X. Zhang, "Workspace mapping method based on edge drifting for the teleoperation system," *J. Phys.: Conf. Ser.*, vol. 2402, no. 1, 2022, Art. no. 012012.

[24] W. Li, F. Huang, Z. Chen, and Z. Chen, "Automatic-switching-based teleoperation framework for mobile manipulator with asymmetrical mapping and force feedback," *Mechatronics*, vol. 99, 2024, Art. no. 103164.

[25] J. I. Mulero-Martínez, "Uniform bounds of the Coriolis/centripetal matrix of serial robot manipulators," *IEEE Trans. Robot.*, vol. 23, no. 5, pp. 1083–1089, Oct. 2007.

[26] E. Slawiñski and V. Mut, "PD-like controllers for delayed bilateral teleoperation of manipulators robots," *Int. J. Robust Nonlinear Control*, vol. 25, no. 12, pp. 1801–1815, 2015.

[27] D. D. Santiago, E. Slawinski, and V. Mut, "Human-inspired stable bilateral teleoperation of mobile manipulators," *ISA Trans.*, vol. 95, pp. 392–404, 2019.

[28] P. Gierlak and M. Szuster, "Adaptive position/force control for robot manipulator in contact with a flexible environment," *Robot. Auton. Syst.*, vol. 95, pp. 80–101, 2017.

[29] C. C. Cheah and Y. Zhao, "Inverse Jacobian regulator for robot manipulator: Theory and experiment," in *Proc. IEEE 43rd Conf. Decis. Control*, 2004, pp. 1252–1257.

[30] H. Sadeghian, L. Villani, M. Keshmiri, and B. Siciliano, "Task-space control of robot manipulators with null-space compliance," *IEEE Trans. Robot.*, vol. 30, no. 2, pp. 493–506, Apr. 2014.

[31] A. Colomé and C. Torras, "Closed-loop inverse kinematics for redundant robots: Comparative assessment and two enhancements," *IEEE/ASME Trans. Mechatron.*, vol. 20, no. 2, pp. 944–955, Apr. 2015.

FERNANDO A. CHICAIZA received the B.Eng. degree in electronics and instrumentation from the Army Forces University—ESPE, Sangolquí, Ecuador, in 2015.

He is a Cisco Certified Network Associate and has worked and collaborated in universities and research centers in Ecuador. He is currently a Ph.D. Fellow with the Instituto de Automática, UNSJ-CONICET, San Juan, Argentina, supported by the German Academic Exchange Service (DAAD) and by the National Scientific and Technical Research Council (CONICET), Argentina. His research interests include robotics, teleoperated and automatic control systems, human–robot interaction, and routing and switching technologies.

EMANUEL SLAWIÑSKI received the Ph.D. degree in control systems engineering from National University of San Juan (UNSJ), San Juan, Argentina, in 2006.

He is currently a Researcher with the National Council of Scientific and Technical Investigations of Argentina (CONICET) and a Professor with UNSJ. His research interests include delayed bilateral teleoperation systems, human factors, haptic feedback, human–robot interaction, and robots' control.

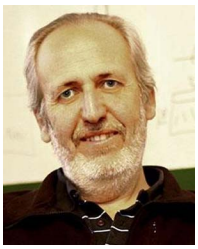

VICENTE MUT received the doctoral degree in engineering of systems of control from the National University of San Juan, San Juan, Argentina, in 1995.

He is currently a Professor with the National University of San Juan and a Principal Researcher with the National Scientific and Technical Research Council (CONICET), Buenos Aires, Argentina, developing research activities and teaching at the graduate and postgraduate programs. He has been qualified as Researcher Class I in the categorization for incentives program to the Research-Education of the Argentinean government. His research interests include robotics, manufacturing systems, adaptive control, and artificial intelligence applied to automatic control.